



# Tectonics

## RESEARCH ARTICLE

10.1002/2016TC004161

### Key Points:

- Thermal-compositional lithospheric structure of the India-Eurasia collision zone
- Identified lateral variations in the lithospheric mantle compositions
- Different lithospheric domains have been identified in the India-Eurasia collision zone

### Supporting Information:

- Supporting Information S1
- Supporting Information S2

### Correspondence to:

L. Tunini,  
ltunini@ictja.csic.es;  
lavinia.tunini@gmail.com

### Citation:

Tunini, L., I. Jiménez-Munt, M. Fernandez, J. Vergés, A. Villaseñor, M. Melchiorre, and J. C. Afonso (2016), Geophysical-petrological model of the crust and upper mantle in the India-Eurasia collision zone, *Tectonics*, 35, doi:10.1002/2016TC004161.

Received 23 FEB 2016

Accepted 29 JUN 2016

Accepted article online 4 JUL 2016

## Geophysical-petrological model of the crust and upper mantle in the India-Eurasia collision zone

Lavinia Tunini<sup>1</sup>, Ivone Jiménez-Munt<sup>1</sup>, Manel Fernandez<sup>1</sup>, Jaume Vergés<sup>1</sup>, Antonio Villaseñor<sup>1</sup>, Massimiliano Melchiorre<sup>1</sup>, and Juan Carlos Afonso<sup>2</sup>

<sup>1</sup>Institute of Earth Sciences Jaume Almera, CSIC, Barcelona, Spain, <sup>2</sup>GEMOC-CCFS Department of Earth and Planetary Sciences, Macquarie University, North Ryde, New South Wales, Australia

**Abstract** We present a new crust and upper mantle cross section of the western India-Eurasia collision zone by combining geological, geophysical, and petrological information within a self-consistent thermodynamic framework. We characterize the upper mantle structure down to 410 km depth from the thermal, compositional, and seismological viewpoints along a profile crossing western Himalayan orogen and Tibetan Plateau, Tarim Basin, Tian Shan, and Junggar Basin, ending in the Chinese Altai Range. Our results show that the Moho deepens from the Himalayan foreland basin (~40 km depth) to the Kunlun Shan (~90 km depth), and it shallows to less than 50 km beneath the Tarim Basin. Crustal thickness between the Tian Shan and Altai mountains varies from ~66 km to ~62 km. The depth of the lithosphere-asthenosphere boundary (LAB) increases from 230 km below the Himalayan foreland basin to 295 km below the Kunlun Shan. To NE the LAB shallows to ~230 km below the Tarim Basin and increases again to ~260 km below Tian Shan and Junggar region and to ~280 km below the Altai Range. Lateral variations of the seismic anomalies are compatible with variations in the lithospheric mantle composition retrieved from global petrological data. We also model a preexisting profile in the eastern India-Eurasia collision zone and discuss the along-strike variations of the lithospheric structure. We confirm the presence of a noticeable lithospheric mantle thinning below the Eastern Tibetan Plateau, with the LAB located at 140 km depth, and of mantle compositional differences between the Tibetan Plateau and the northern domains of Qilian Shan, Qaidam Basin, and North China.

## 1. Introduction

The present-day lithospheric structure of the Himalayan orogen, Tibetan Plateau, and surrounding regions is the result of ~270 Myr long convergence between India and Eurasia plates. The process included different subduction and suturing episodes during the closure of the Neo-Tethys Ocean, which successively accreted continental terrains at the southern border of Asia, and finally culminated with the continental collision between the Indian and Eurasian plates. The collisional process resulted in large amounts of thrusting and crustal thickening along the Himalayan orogen and broadly distributed deformation with the formation of the high Tibetan Plateau and of additional reliefs extending some 2000 km north of Indus-Yarlung Suture, such as the Kunlun Shan and the Tian Shan to the north and the Qilian Shan to the east [Molnar and Tapponnier, 1975; Yin and Harrison, 2000; Tapponnier et al., 2001].

The region has been the subject of numerous ongoing researches but the nature of the deep structure and the mechanism supporting the high Tibetan Plateau are still debated questions. The chemical composition of the lithospheric mantle plays a fundamental role on its buoyancy/rigidity characteristics and its tectonic behavior [Lenardic and Moresi, 1999; Griffin et al., 2009]. The long tectonic evolution of the India-Eurasia collisional system has likely modified the chemical composition of the lithospheric mantle, causing significant changes in the geometry of the crust-mantle and lithosphere-asthenosphere boundaries. Up to date, however, a quantified thermal and petrophysical characterization of the lithospheric mantle in the India-Eurasia collision zone, consistent with geothermobarometers and tomography models, has not been attempted. Previous geophysical studies put efforts in identifying the nature and composition of the deep unexposed crustal parts of the orogen, arguing for the presence of eclogites under Tibet [Schulte-Pelkum et al., 2005; Hetényi et al., 2007], granulite-facies lower crust under the Himalayan orogen [Nelson et al., 1996; Jackson et al., 2004; Groppo et al., 2007; Grujic et al., 2011; Warren et al., 2011], or under southern Tibet [Le Pichon et al., 1999; Priestley et al., 2008]. However, though the contribution of chemical composition and phase transitions on the density and buoyancy of the lithospheric mantle are key aspects on the resulting

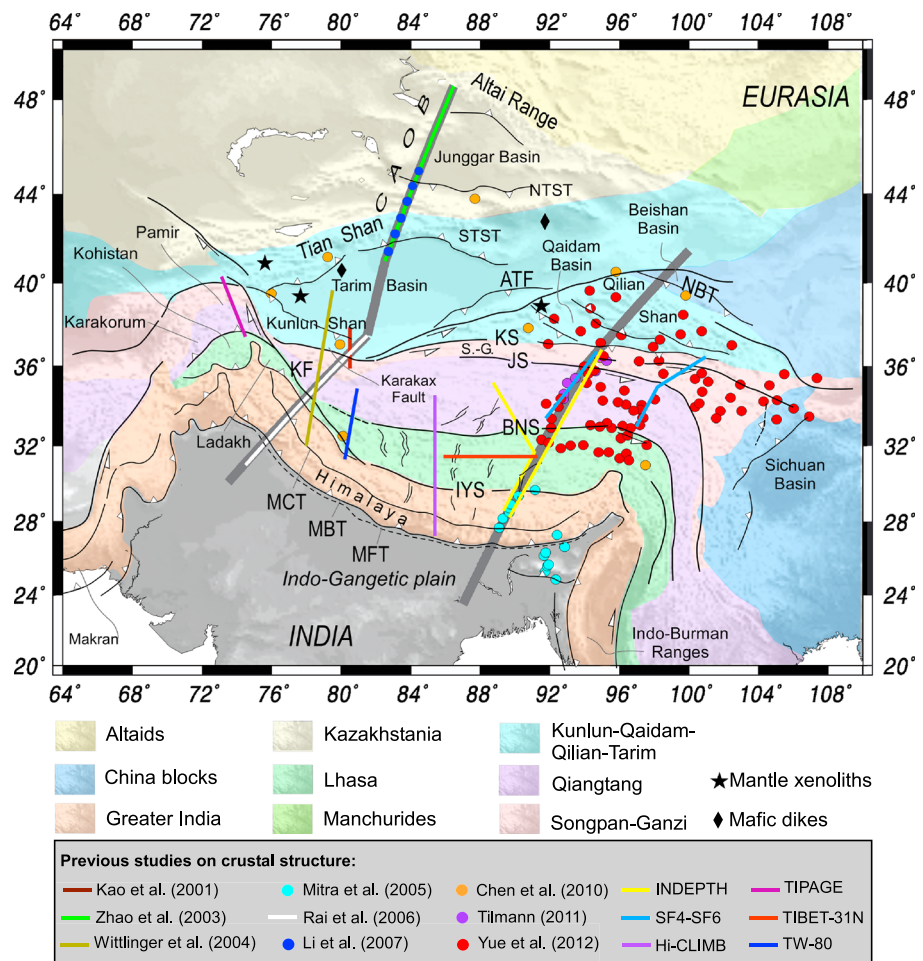


**Figure 1.** Tectonic map of the India-Eurasia collisional system and previous studies on the crustal structure (color-coded symbols). Thick grey lines show the location of A-B and C-D profiles. The names of the different terrains are taken from *van Hinsbergen et al.* [2011]. Black stars indicate mantle xenolith localities: in the western Tian Shan [Bagdassarov et al., 2011], in the western Tarim Basin [Chen et al., 2014], and in Qaidam Basin [Song et al., 2007]. Black rhomboids represent mafic dikes localities from Zhang and Zou [2013]. INDEPTH [Nelson et al., 1996; Zhao et al., 2011]; SF4-SF6, Sino-French passive seismic experiments in 1998 and 1993 [Galvé et al., 2006; Vergne et al., 2002; Jiang et al., 2006]; Hi-CLIMB [Nabelek et al., 2009; Wittlinger et al., 2009]; TIPAGE [Mechie et al., 2012]; TIBET-31 N [Y. Chen et al., 2015]; and TW-80 [Zhang et al., 2014a]. ATF = Altyn Tagh Fault; BNS = Bangong Nujiang Suture; CAOB = Central Asia Orogenic Belt; IYS = Indus-Yarlung Suture; JS = Jinsha Suture; KF = Karakorum Fault; KS = Kunlun Suture; MBT = Main Boundary Thrust; MCT = Main Central Thrust; MFT = Main Frontal Thrust; NBT = North Border Thrust; NTST = Northern Tian Shan Thrust; S-G. = Songpan-Ganzi; and STST = Southern Tian Shan Thrust.

lithospheric structure [Afonso et al., 2008; Fullea et al., 2009], no such analysis has been performed in the western Tibet-Himalaya region.

In this study, we present a new 2-D crustal and upper mantle cross section in the west India-Eurasia collision zone, which crosses from India to Asia, the western Himalayan orogen and Tibetan Plateau, the Tarim Basin, the Tian Shan, and Junggar Basin, ending in the southern edge of the Altai Range (Profile A-B, Figure 1). We apply a finite-element method (LitMod-2D) [Afonso et al., 2008] that uses a self-consistent thermodynamic-geophysical framework in which the mantle properties (density, thermal conductivity, and elastic parameters) are functions of temperature, pressure, and chemical composition. This approach allows defining a geophysical model in which the chemical composition of the lithospheric mantle obtained from laboratory and xenolith analyses is used to derive the most relevant mineral assemblages and to calculate the corresponding geophysical observables. The modeled crust and lithospheric mantle structures are constrained by available data on elevation, Bouguer anomaly, geoid height, surface heat flow, and seismic data including seismic refraction and wide angle reflection, receiver functions, and *P* and *S* wave tomographic models. This

technique has been successfully applied in other collisional settings, such as in the Iberian Peninsula along three regional cross sections [Carballo *et al.*, 2015a, 2015b; Pedreira *et al.*, 2015] and across the Zagros Mountains and Iranian Plateau [Tunini *et al.*, 2015].

We also modeled the lithospheric profile by Jiménez-Munt *et al.* [2008] with this new technique to discuss the along strike variations of the lithospheric structure. This profile crosses the eastern Himalayan orogen and Tibetan Plateau, the Qaidam Basin, the Qilian Shan, and Beishan units, ending in the North China cratonic block (Profile C-D, Figure 1). The results obtained along the two transects allows us to (i) analyze the effect of the mantle composition on the lithospheric structure, (ii) discuss consistently the differences between the eastern and western India-Eurasia collision zone in terms of lithospheric mantle composition and thickness, and (iii) compare the calculated *P* and *S* velocity distributions in the upper mantle with published seismic tomography studies.

## 2. Geological Background

The India-Eurasia collision zone consists of a large amalgamation of crustal and lithospheric domains, accreted each other throughout time. The India peninsula is formed by an ancient continental crust (the Precambrian Indian shield), which is itself a collage of cratonic blocks and mobile belts assembled between mid-Archean and neo-Proterozoic times. The Himalayan orogen (Figure 1) corresponds to the ancient northern margin of the Indian plate, strongly deformed in three major tectonic units: the Lesser Himalaya, the Greater Himalaya, and the Tethys Himalaya. These units are separated from each other by major crustal-scale thrusts, named, from south to north: (1) Main Frontal Thrust (MFT), carrying the Neogene molasses of the Siwalik units over the Indo-Gangetic plain; (2) Main Boundary Thrust (MBT), carrying the Lesser Himalaya sequence over the Neogene molasses; (3) Main Central Thrust (MCT), separating the gneisses and migmatites of the Greater Himalaya from the Lesser Himalaya units; (4) the Zaskar Shear Zone (ZSZ), a low angle normal fault separating the Greater Himalayan sequence and the overlain Tethys sedimentary sequence; and (5) Indus-Yarlung Suture (IYS), representing the suture zone between India and Eurasia plates, including ophiolites, deep sea sediments deposited on the Neo-Tethys Ocean floor, and Mesozoic island-arc volcanic rocks.

North of the IYS, the Lhasa block is the southernmost continental terrain accreted along the southeastern Eurasia margin. It consists of a ~300 km wide tectonic domain narrowing westward and is formed by sedimentary sequences ranging from Ordovician to Triassic and a mid-Proterozoic to early Cambrian basement [Yin and Harrison, 2000]. The Lhasa block collided with the Qiangtang terrain in the Jurassic [Dewey *et al.*, 1988], along the Bangong-Nujiang Suture (BNS). The Qiangtang terrain forms a strip of 1900 km long and ~300 km wide, delimited by the BNS to the south and by the Jinsha Suture (JS) to the north. This terrain consists of Triassic to Jurassic sequences composed of metamorphosed mélange complexes, shallow marine carbonates interbedded with nonmarine clastic and volcanoclastic deposits [Liu, 1988], and intruded granitoids 111–145 Ma [Yin and Harrison, 2000]. North of the JS, there is a relatively heterogeneous zone, which to the west is bounded by the Altyn Tagh Fault (ATF) and its western continuation, the Karakax Fault. These two large faults separate the microterrains of the Eastern Tibetan Plateau and the Kunlun Shan from the rigid Tarim block [Searle, 2010]. Approximately at 76°E longitude, the IYS zone bounds two parallel ranges, the Ladakh and the Karakorum, which are the westward prolongations of the Lhasa and Qiangtang terrains, respectively. The Ladakh batholith forms a 500 km long and 25 km wide belt in continuity with the Kohistan arc, an accreted island arc between the Indian and Eurasian plates (see Figure 1 for location). The Shyok Suture marks its northern limit, with the Karakorum thrust on top of the Kohistan and Ladakh units. The Ladakh is a Cretaceous-Early Tertiary batholith, composed by sheared greenschists grading to basalts and granitoids, an andesitic unit, and plutonic rocks ranging from gabbro and diorite, to granodiorite and leucogranites showing calc-alkaline geochemical affinities. In this region, the Western Tibetan Plateau, composed by the Ladakh and the Qiangtang, is less than 350 km wide, nearly the half of the Eastern Tibetan Plateau. The Tarim Basin, covering an area of nearly 600,000 km<sup>2</sup>, is the largest cratonic domain in western China. Its Precambrian crystalline basement is inferred to be a fragment of the Rodinia Supercontinent [Lu *et al.*, 2008, and references therein]. It is covered by a thick (4–12 km) [Gao and Ye, 1997, Figure 2] sedimentary sequence containing Ordovician, Permian, and Cretaceous strata. The Permian units consist of volcano-sedimentary sequences derived from large flood basalts which affected the so-called Tarim Large Igneous Province ~290 Ma (i.e., the Tarim Basin and the western part of the Central Asian

Orogenic Belt—CAOB—including the Tian Shan, Junggar region, and Altai; Figure 1) [Xu *et al.*, 2014]. Despite the Permian magmatic event, the evolution of the Tarim Basin is characterized by almost continuous sedimentation since the Neo-Proterozoic [Xu *et al.*, 2014], whereas the CAOB experienced subduction and accretion-related processes through the Paleozoic, being finally amalgamated with the Tarim craton in the Late Carboniferous [Wang *et al.*, 2006; C. L. Zhang *et al.*, 2012].

The central-eastern sector of the Tibetan Plateau, from the JS northward, is formed by (i) the Songpan-Ganzi terrain, formed by a thick sequence of deep marine Triassic strata; (ii) the eastern Kunlun-Qaidam terrain and the Qaidam Basin, bounded to the north by the southern Qilian Suture and dominated, to the south, by a broad Early Paleozoic arc, on which a younger and narrower Late Permian to Triassic arc was superposed [Harris *et al.*, 1988; Jiang *et al.*, 1992]; and (iii) the Qilian Shan, formed by complexly deformed Early Paleozoic arcs, which developed at the southern margin of the North China craton before it was offset by the Altyn Tagh Fault during the Cenozoic [Yin and Harrison, 2000].

### 3. Method

We used a 2-D numerical code (LitMod-2D) [Afonso *et al.*, 2008], which combines geophysical and petrological data to infer the crustal and upper mantle structure down to 410 km depth. The code calculates the 2-D distribution of temperature, density, and mantle seismic velocities and the resulting surface heat flow, elevation, gravity, and geoid anomalies. LitMod-2D works under a forward modeling scheme; at each step, the model outputs (elevation, gravity and geoid anomalies, surface heat flow, and mantle seismic velocities) are compared with observed data (geophysical observables, seismic velocities, and tomography images) and the input parameters and model geometry can be modified by the user within the experimental uncertainties, in a trial and error procedure until the best fitting model is obtained. The model domain is composed of multiple polygons, representing the different crustal and mantle bodies, to which a triangular finite element mesh is adapted. In this study, the horizontal grid is 10 km, and the vertical varies between 500 m at shallow levels and 10 km below 250 km.

Each crustal body is associated with a single lithology, described by a set of thermophysical parameters, i.e., density, thermal conductivity, and radiogenic heat production. Density and thermal conductivity can be pressure and temperature dependent, whereas radiogenic heat production can be either constant or exponentially decreasing with depth. The geometry and properties of the crustal bodies are assigned according to the geological structure and constrained by existing data.

Each mantle body is characterized by its main oxides composition (in wt %) within the NCFMAS ( $\text{Na}_2\text{O}$ - $\text{CaO}$ - $\text{FeO}$ - $\text{MgO}$ - $\text{Al}_2\text{O}_3$ - $\text{SiO}_2$ ) system. Stable mineral assemblages in the mantle are calculated using a Gibbs free energy minimization procedure as described by Connolly [2005]. The resulting thermodynamic tables are generated by Perple-X [Connolly, 2005], describing densities, elastic, and thermophysical parameters of the end-member minerals. Thus, physical properties of each mineral and of the bulk mantle bodies (density, thermal expansion coefficient, seismic velocities, and thermal conductivity) are modeled consistently as a function of temperature, pressure, composition, and phase changes, rather than as a function of only temperature as in previous methodologies. In this work, we use an augmented-modified version of Holland and Powell [1998] (revised in 2002) thermodynamic database [see Afonso and Zlotnik, 2011]. Density and seismic velocities in the mantle are determined according to the elastic moduli and density of each end-member mineral, as described in Afonso *et al.* [2008]. Anelastic effects are computed applying a pressure-temperature-dependent correction to the output anharmonic velocities [Karato, 1993; Afonso *et al.*, 2005]. In this study we selected a grain size of 5 mm for the mantle, in agreement with previous studies [Afonso *et al.*, 2008; Carballo *et al.*, 2015a]. The lithospheric mantle composition can vary laterally depending on the geodynamic context of a certain region, whereas the asthenosphere is considered homogeneous in composition, due to its convective nature. Litmod assumes that the asthenospheric mantle has the primitive upper mantle (PUM) composition of McDonough and Sun [1995]. In order to smooth the compositional change between the lithospheric mantle and the underlying asthenosphere, we introduced a layer of 10–20 km thickness with an intermediate composition between the asthenosphere and the overlying lithospheric mantle.

The lithosphere is considered the colder outermost layer of the Earth in which the heat transfer is dominated by conduction [Schubert *et al.*, 2001], and its base is defined as an isothermal boundary. Therefore, the heat transport equation is solved for the lithosphere by finite element method under a steady state regime and



assuming a purely conductive behavior. The boundary conditions are (i) 0°C at the model surface, although surface temperatures in the range of 0–20°C do not affect the results significantly [see Afonso *et al.*, 2008]; (ii) no horizontal heat flow across the lateral boundaries of the model; and (iii) 1320°C at the lithosphere–asthenosphere boundary (LAB). Below the lithosphere, the temperature evolves following an adiabatic gradient. The temperature at the bottom of the model (410 km) is constant to 1520°C if the condition of the adiabatic gradient in the sublithospheric mantle is between 0.35 and 0.50°C/km. If not, the basal temperature will change according to this adiabatic gradient limitation. To avoid unrealistic discontinuities in the geothermal gradient we define a thermal buffer beneath the LAB with a thickness of 40 km and a temperature at its bottom of 1400°C. This buffer mimics the thermal effect of a rheologically active layer present at the bottom of the upper thermal boundary layer in convecting mantle-like fluids [Afonso *et al.*, 2008; Fullea *et al.*, 2009]. Mantle thermal conductivity is calculated as a function of composition, temperature, and pressure following Grose and Afonso [2013]. Gravity and geoid calculations are performed by using simple algorithms applied to the elements of the mesh, and elevation is calculated at each column of the mesh under the assumption of local isostasy (see Zeyen *et al.* [2005] for further details). Flexural effects related to regional isostasy can be noticeable at length scales <200 km [England and Molnar, 1997], though the gravity field in Tibet indicates that the topography there is for the most part in local isostatic equilibrium [Jin *et al.*, 1994]. On the other hand, isostasy, local or regional, ignores the possible effects of dynamic topography associated with sublithospheric mantle flow. Husson *et al.* [2014] have estimated the transient dynamic topography produced by the subduction of the Tethys oceanic plate between India and Central Asia. These authors conclude that the dynamic contribution to elevation changed through time producing subsidence (4–5 km when sediment load is considered) in the Indo-Gangetic Plain from 15 to 0 Ma, and uplift (~1 km) in the Himalaya–Tibet belt from 25 to 15 Ma. According to these calculations, the effects of the present-day dynamic topography along our model profiles amount few tens of meters in the flanks of the Indo-Gangetic Plain and across the Himalaya–Tibetan belt, and therefore, they are negligible.

In this study, improvements have been implemented to the code, in order to take into account processes like subduction or slab detachment: (i) physical perturbations within the sublithospheric mantle, either of thermal or compositional nature, can be now incorporated in the model and (ii) these sublithospheric perturbations can be either coupled (i.e., considering that density anomalies are transmitted to surface elevation) or decoupled (i.e., when density anomalies are not transmitted to surface elevation). Decoupled bodies do not have effects on calculated topography but they do on gravity/geoid calculations. We define the sublithospheric anomalies as coupled or decoupled according to the geodynamic context.

Finally, the crustal model is fixed by previous published data (e.g., geological cross sections, seismic profiles, gravimetry, and magnetotellurics), and it is slightly modified only within the uncertainty of these data during the modeling procedure. The resulting crust and LAB geometries adjust simultaneously topography, geoid, gravity, thermal data, and seismic velocities following a trial and error procedure.

## 4. Data

The data used to constrain the models are (1) regional surface geophysical observables (elevation, surface heat flow, and potential field data) collected from global databases; (2) results on the crustal and lithospheric mantle structure from previous studies; (3) *P* wave tomography inferred from a global tomography model obtained using the same method described in Bijwaard *et al.* [1998], but using a much larger arrival time data set [Villaseñor *et al.*, 2003]; and (4) lithospheric mantle compositions consistent with the lithospheric age and with the geochemistry of mantle xenolith suites (see reference in section 4.4).

### 4.1. Regional Geophysical Data

Elevation data (Figure 2a) come from 1 min arc resolution ETOPO1 global elevation model [Amante and Eakins, 2009]. The topography of the region is highly variable and characterized by steep gradients separating the topographic domains. The major flat areas, Tibetan Plateau, Tarim, and Junggar basins, are surrounded by six different mountain ranges: the Himalaya and Karakorum ranges, with an average elevation of 4000–5000 m and several peaks over the 8000 m; the Tian Shan (~4000 m) and the Qilian Shan (~4500 m), located to the north and to the east of the Tarim Basin, respectively; the Kunlun Shan (~4000 m), located at the southern border near the Pamir region; and the Altai Range (2500–3000 m) extending to the northern and eastern border of the Junggar Basin.

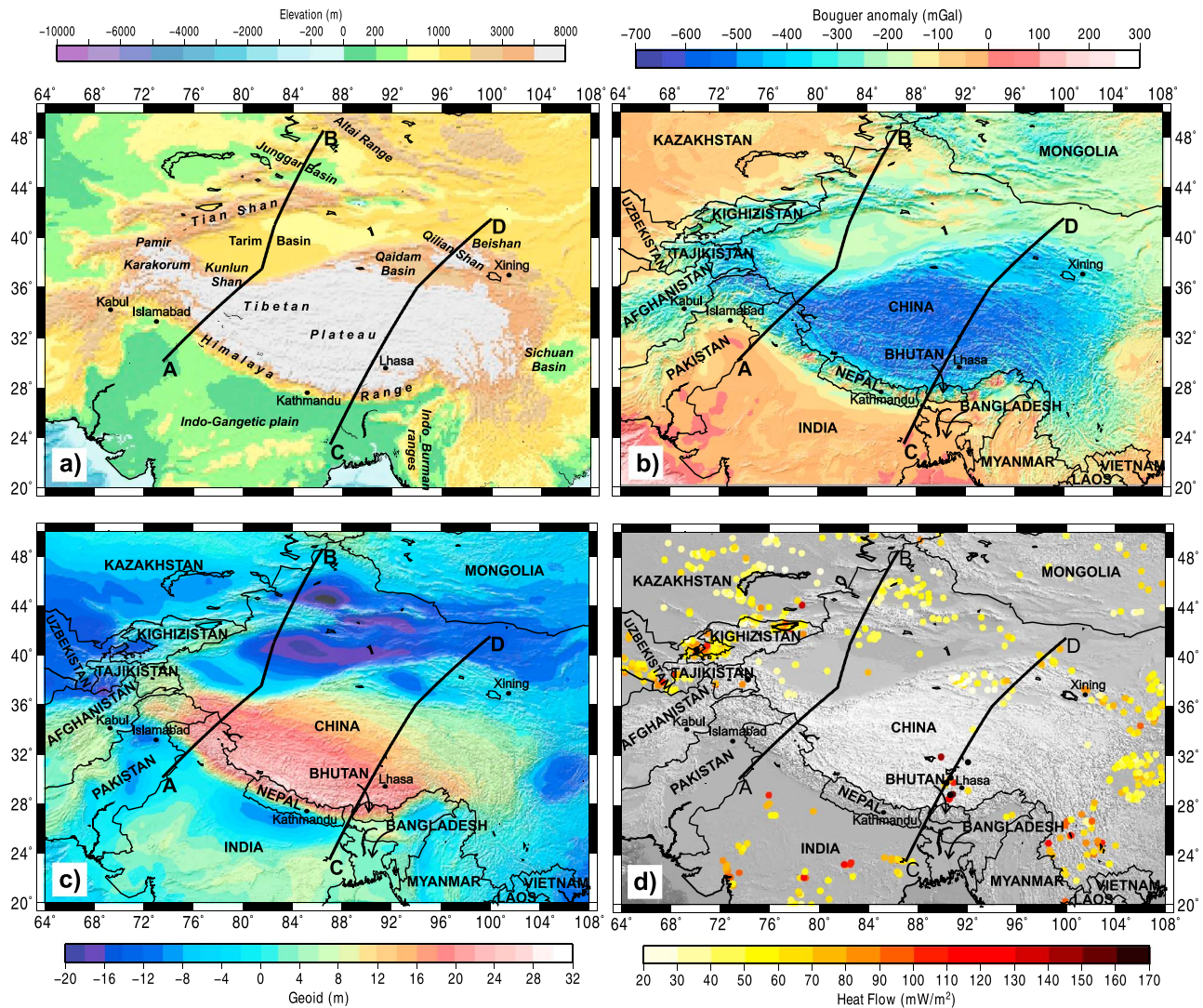


**Figure 2.** Geophysical observables in the study region. (a) Topography; (b) Bouguer anomaly calculated from global free-air anomaly [Sandwell and Smith, 1997] with 3-D topographic correction; (c) geoid height from EGM2008 model filtered to degree and order 9; and (d) heat flow measurements from global data set [Pollack et al., 1993].

The Bouguer anomaly (Figure 2b) has been computed applying the complete Bouguer correction to 1 min grid of satellite free-air data [Sandwell and Smith, 1997] using the FA2BOUG software [Fullea et al., 2008] and a reduction density of  $2670 \text{ kg/m}^3$ . A strongest negative Bouguer anomaly of  $-500 \text{ mGal}$  characterizes the entire Tibetan Plateau and the Himalaya-Karakorum ranges, gently smoothing toward the syntaxes, the Pamir and Beishan regions. The Tian Shan and Altai Range are characterized by values of  $\sim -300 \text{ mGal}$ , whereas the Tarim and Junggar basins show values between  $-100$  and  $-200 \text{ mGal}$ . Positive anomalies are only observed in the Indo-Gangetic plain ( $\sim 50 \text{ mGal}$ ).

Geoid height data (Figure 2c) derive from the Earth Geopotential Model EGM2008 [Pavlis et al., 2008], with  $1 \times 1 \text{ min}$  grid gravity anomaly data including spherical harmonic coefficients up to degree and order 2190. According to Bowin [2000], wavelengths larger than  $4000 \text{ km}$  were removed subtracting spherical harmonics up to degree and order 9 to obtain a residual geoid anomaly that reflects the density distribution of the first  $\sim 400 \text{ km}$  of depth. The highest geoid height is observed along the Himalayan orogen ( $\sim 30 \text{ m}$ ), gradually decreasing toward the Beishan and toward the Karakorum. Minimum values are in the central Junggar Basin ( $\sim -22 \text{ m}$ ) and in the Tarim Basin (values between  $\sim -10 \text{ m}$  in the northeastern sector and  $\sim -2 \text{ m}$  in the southwest).

Surface heat flow data (Figure 2d) are taken from the global compilation by *Pollack et al.* [1993]. In general, details on the quality data are not available from referred works. According to the International Heat Flow Commission, the good, average, and poor accuracy levels are, respectively, of  $\pm 5$ , 10, and 20%. Heat flow values in the Tarim and Qaidam basins, Qilian Shan, and Tian Shan are between  $40 \text{ mW/m}^2$  and  $70 \text{ mW/m}^2$ , increasing westward toward the Pamir where values of  $100\text{--}120 \text{ mW/m}^2$  are measured. In the Tibetan Plateau heat flow data are very scarce and show a high scatter, probably related to active groundwater flow and/or crustal melting as evidenced by the presence of numerous geysers, hot springs, volcanic, and anhydrous xenoliths [*Nelson et al.*, 1996; *Hacker et al.*, 2000; *Jiménez-Munt et al.*, 2008]. The few available data indicate high heat flow in eastern Lhasa terrain, with values between  $180 \text{ mW/m}^2$  and  $194 \text{ mW/m}^2$ . Few and sparse additional data show values of  $\sim 60 \text{ mW/m}^2$  in the western Himalayan orogen [*An and Shi*, 2007],  $55\text{--}60 \text{ mW/m}^2$  in the Western Tibetan Plateau [*An and Shi*, 2007],  $44\text{--}55 \text{ mW/m}^2$  in the Tarim Basin [*Wang*, 2001; *An and Shi*, 2007],  $50\text{--}58 \text{ mW/m}^2$  in the Tian Shan [*Wang*, 2001; *An and Shi*, 2007],  $\sim 52 \text{ mW/m}^2$  in the Junggar Basin [*Wang*, 2001], and  $\sim 46 \text{ mW/m}^2$  in the Altai Range [*Wang*, 2001]. These data are not included in Figure 2d because they correspond to average regional values, though we include them for comparison with the obtained results (see section 5).

#### 4.2. Previous Studies on the Crustal and Lithospheric Mantle Structure

During the last three decades a large amount of geologic and geophysical investigations has been carried out in the Himalayan-Tibetan region mainly to image the crustal structure: the broadband seismic experiments PASSCAL [e.g., *Owens and Zandt*, 1997; *McNamara et al.*, 1997] and TW-80 [*Zhang et al.*, 2014a], the international and multidisciplinary experiments INDEPTH [e.g., *Nelson et al.*, 1996; *Zhao et al.*, 2011], Hi-CLIMB [e.g., *Nabelek et al.*, 2009; *Wittlinger et al.*, 2009] and Xayar-Burjing Geoscience transect [*Zhao et al.*, 2003], the series of Sino-French seismic studies [e.g., *Galvé et al.*, 2006; *Jiang et al.*, 2006], the TIPAGE wide-angle seismic project [*Mechie et al.*, 2012], the TIBET-31N seismic array [*Y. Chen et al.*, 2015], magneto-telluric [e.g., *Zeng et al.*, 2015], gravimetry [e.g., *Braitenberg et al.*, 2000, 2003; *Steffen et al.*, 2011; *He et al.*, 2014], receiver functions [e.g., *Wittlinger et al.*, 2004; *Mitra et al.*, 2005; *Hetényi et al.*, 2007; *Rai et al.*, 2006; *Chen et al.*, 2010; *Shi et al.*, 2015], joint inversion of elevation, geoid with thermal analysis [*Robert et al.*, 2016], and combining teleseismic and gravity [*Basuyau et al.*, 2013].

*Li et al.* [2006] summarize the results of about 90 seismic refraction/wide-angle reflection profiles in a crustal thickness map of the mainland China. The map shows values of  $70\text{--}74 \text{ km}$  in the southern Tibetan Plateau,  $60\text{--}68 \text{ km}$  in the Himalayan and Qiangtang regions, gradually decreasing to  $48 \text{ km}$  toward the northeast (Qaidam Basin, Qilian Shan, and Beishan Basin). Minimum values of crustal thickness are found in the Tarim ( $\sim 44 \text{ km}$  in its middle central zone) and Junggar ( $42\text{--}44 \text{ km}$ ) basins, whereas the Tian Shan is modeled with a  $52\text{--}54 \text{ km}$  thick crust. Seismic studies show that after a progressive deepening of the Moho from  $\sim 40 \text{ km}$  beneath the Himalayan foreland basin to  $\sim 90 \text{ km}$  beneath the western Qiangtang and Kunlun Shan [*Rai et al.*, 2006], a remarkable Moho step [ $\sim 20 \text{ km}$ , *Wittlinger et al.*, 2004;  $\sim 30 \text{ km}$ , *Rai et al.*, 2006; *Zhao et al.*, 2010] indicates the transition to the Tarim Basin, characterized by  $50\text{--}60 \text{ km}$  thick crust [*Kao et al.*, 2001; *Wittlinger et al.*, 2004; *Rai et al.*, 2006]. These values are also consistent with those obtained by inverting the most recent gravity data (from GRACE and GOCE satellite missions), which show a crustal thickness sharply decreasing from  $\sim 70 \text{ km}$  in the Western Tibetan Plateau to  $35\text{--}47 \text{ km}$  in the Tarim Basin [*Shin et al.*, 2007; *Tenze et al.*, 2014]. Farther north, *Zhao et al.* [2003] carried out an extensive study with wide-angle seismic reflection/refraction surveys, magneto-telluric sounding, and 2-D density structure analysis across the Tian Shan and Altai Range. The results reveal the complexity of the crust-mantle transition zone beneath the Tian Shan, characterized by an interdigitated structure involving the upper, middle, and lower crust layers. The crust-mantle boundary is located at depths of about  $64 \text{ km}$  beneath the Tian Shan,  $55 \text{ km}$  in the Junggar Basin, and  $60 \text{ km}$  in the southern Altai Range. Another seismic experiment imaged the Moho discontinuity across the Tian Shan, from the northern Tarim Basin to the Junggar Basin [*Li et al.*, 2007]. The profile shows an averaged crustal thickness of  $48 \text{ km}$  in the Tarim Basin,  $55\text{--}60 \text{ km}$  in the Tian Shan, and  $50 \text{ km}$  in the southern Junggar Basin. The estimated resolution in Moho depth depends on the seismic acquisition technique being of about  $\pm 5 \text{ km}$  for receiver functions and  $\pm 3 \text{ km}$  for seismic refraction and wide-angle seismic reflection.

The lithospheric mantle structure is harder to constrain, due to the lack of direct observables and to its strong dependence on the lithosphere definition (seismic/thermal/elastic lithosphere) [e.g., *Eaton et al.*, 2009; *Artemieva*, 2011]. A source of information about the upper mantle structure comes from seismic tomography



studies, which denotes east-west variations of the velocity anomalies across the Tibetan Plateau [Van der Voo *et al.*, 1999; Zhou and Murphy, 2005; Huang and Zhao, 2006; Li *et al.*, 2008; H. Zhang *et al.*, 2012; Replumaz *et al.*, 2014; Mohanty *et al.*, 2016]. The tomography profiles show a fast velocity feature, interpreted as the Indian lithosphere underthrusting south Tibet, and a low velocity zone in NE Tibet [e.g., Zhao *et al.*, 2010].

Receiver function profiles image the lithosphere-asthenosphere boundary below the Western Tibetan Plateau at 180–220 km depth, deepening westward toward the Karakorum and Pamir regions [Zhao *et al.*, 2010]. A jump in the LAB depth of ~50 km marks the transition from the deeper Indian LAB to the shallower Eurasian LAB [Zhao *et al.*, 2010]. Consistently to these results, *P* and *S* wave tomography studies show that the LAB below the Tarim Basin is relatively shallower with respect to the Indian one and located at 150–200 km depth [Xu *et al.*, 2002; An and Shi, 2006; Priestley and McKenzie, 2006; Lei and Zhao, 2007]. Northward, the Tian Shan belt is characterized by an even thinner lithosphere [120–170 km, Xu *et al.*, 2002; 90–120 km, Kumar *et al.*, 2005], with higher temperatures (~1390°C at 150 km depth) [An and Shi, 2006] and low velocities penetrating in the lower crust, which have been related to the upwelling of hot mantle anomalies [Xu *et al.*, 2002, and references therein; Lei and Zhao, 2007].

### 4.3. *P* Wave Tomography Profile of the Western India-Eurasia Collision Zone

We present a vertical cross section (Figure 3a) of a *P* wave global tomographic model obtained using the same method described in Bijwaard *et al.* [1998] but using a much larger arrival time data set [Villaseñor *et al.*, 2003]. This data set incorporates additional earthquakes from 1995 to 2002 listed in the International Seismological Centre's bulletins and arrival times recorded at regional distances that were not used previously. In total, more than 14 million arrival times from 300,000 earthquakes, nearly 4 times the amount used by Bijwaard *et al.* [1998], were reprocessed using the EHB methodology [Engdahl *et al.*, 1998]. The ray paths corresponding to these new arrival times sample mainly the uppermost mantle and it is in this region where the resolving power of the new data set is increased, allowing to image seismic velocity anomalies of the same resolution of the grid used for the tomographic inversion ( $0.5^\circ \times 0.5^\circ$  in area and 25–50 km in depth). Figure 3b shows a synthetic reconstruction test with anomalies of  $2^\circ \times 2^\circ$  with alternating positive and negative values separated by a  $2^\circ$  buffer with 0% anomaly. For the two upper mantle depth slices shown, the reconstruction is good throughout the study region.

The tomography image shows a strong positive anomaly (up to 4%) beneath the Himalayan orogen and the Himalayan foreland basin, vanishing to about 300 km depth. *P* wave anomalies show progressive lower amplitudes northeastward, i.e., up to 2% below the Tarim Basin, and  $\leq 1\%$  in the Tian Shan, Junggar, and Altai regions. The transition between positive and negative anomaly is located at ~220 km depth beneath the Tarim Basin and ~320 km depth beneath the Tian Shan. In the first 400 km depth of the profile, only one negative anomaly is imaged ( $\leq -1\%$ , between 300 and 400 km depth), beneath the Tarim Basin. Finally, it is worthy to notice a clear decrease in the amplitude of the positive anomaly below the Tarim Basin with respect to the Western Tibetan Plateau and beneath the Junggar Basin, relative to the Tarim or Altai regions. These velocity drops can be the result of either local lithospheric thickness variations (locally thinner lithosphere) or of compositional changes, or more likely a combination of both.

### 4.4. Lithospheric Mantle Composition

Mineral assemblages in the lithospheric mantle have been computed using the NCFMAS-major-oxides approach. On the whole, the bulk composition of the lithospheric mantle is peridotitic. Tectonothermal processes related to progressive basaltic melt extraction can change considerably this average composition from one place to another, consequently affecting the physical properties of the lithospheric mantle. Thus, lithospheric domains with different tectonothermal histories are expected to have different physical properties and chemical compositions. The composition of the lithospheric mantle is broadly dependent upon the age of the overlying crust, being the Archean and Proterozoic cratons the most depleted lithospheric mantle portions [Griffin *et al.*, 1998, 1999; Hawkesworth *et al.*, 1999; Gaul *et al.*, 2000; Zheng *et al.*, 2001; O'Reilly *et al.*, 2001]. Global data from mantle-derived xenoliths and garnet xenocrysts in volcanic rocks and exposed orogenic peridotite massifs document a secular compositional evolution of the lithospheric mantle, revealing a depletion in Fe, Ca, and Al contents from Archean to Phanerozoic times [Griffin *et al.*, 2003, 2009; O'Reilly and Griffin, 2006; Poudjom-Djoman *et al.*, 2001]. The chemical composition of the lithospheric mantle, especially in terms of Fe and Al contents, has important consequences for geophysical properties. Low content of Fe



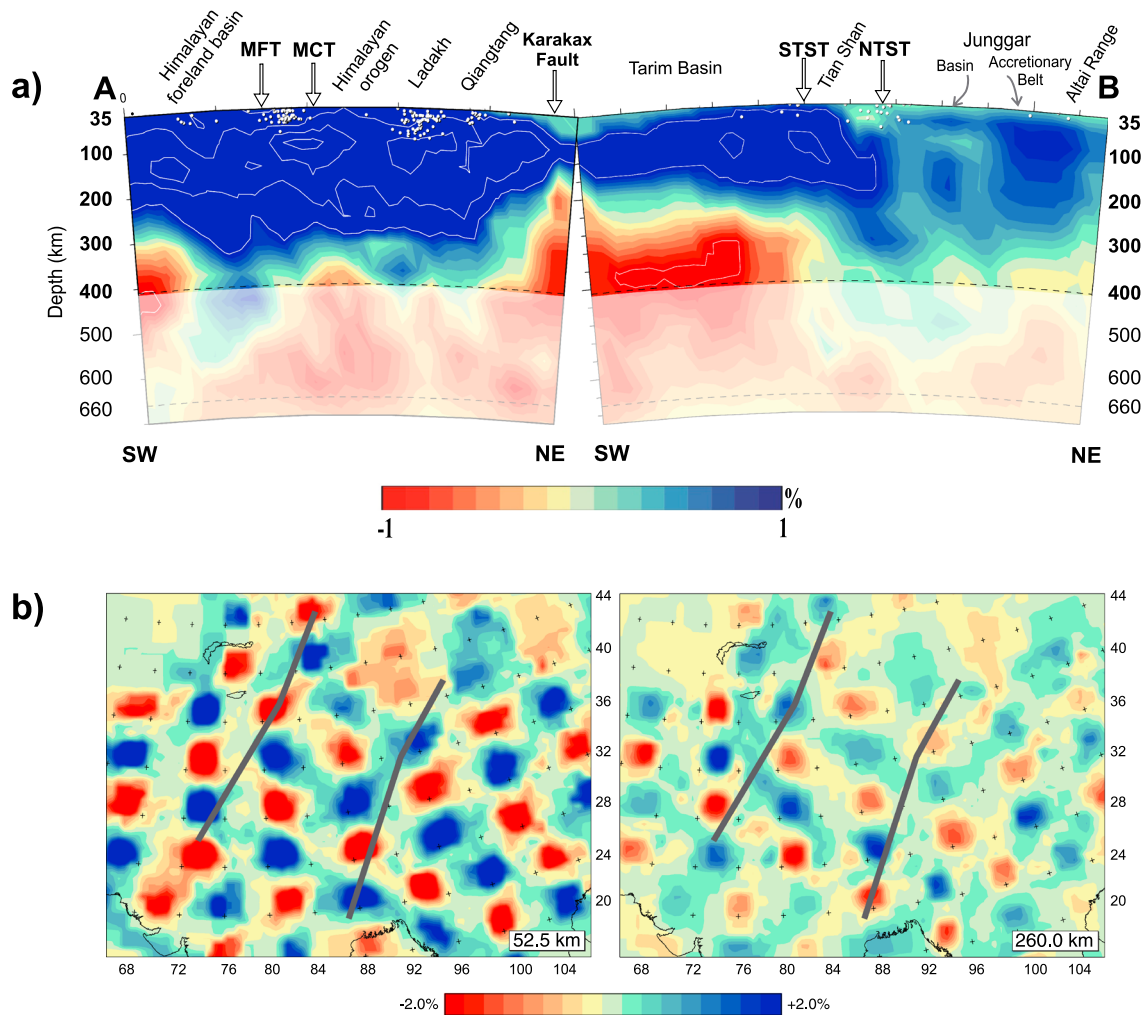


**Figure 3.** (a) *P* wave seismic tomography image along A-B profile (see location in Figure 1). White circles represent the earthquakes used in the tomography [Engdahl *et al.*, 1998]. Contour lines interval: 1%. Global reference model used—AK135 [Kennett *et al.*, 1995]. MCT = Main Central Thrust; MFT = Main Frontal Thrust; NTST = Northern Tian Shan Thrust; and STST = Southern Tian Shan Thrust. (b) Results of spike reconstruction tests of the *P* wave tomographic model of Villaseñor *et al.* [2003] for two upper mantle depths: 35–70 km (left) and 230–290 km (right). The synthetic model consists of spike anomalies of  $2 \times 2^\circ$  with alternating positive and negative anomalies of  $\pm 5\%$  separated by a  $2^\circ$  buffer with 0% anomaly.

results in lower densities and higher seismic velocities [Artemieva, 2006; Poudjom-Djomani *et al.*, 2001], meanwhile high content of Al results in high seismic velocities.

Three mantle xenoliths and two magmatic dikes localities have been analyzed in the study area (Figure 1). In the Tian Shan, geochemical data are available from the xenolith analyses by Bagdassarov *et al.* [2011]. In the Tarim Basin, mantle xenolith suites [Chen *et al.*, 2014] suggest that the lithospheric mantle is formed by, at least partly, juvenile mantle material related to the Early Permian mantle plume event, which caused flood basalt magmatism covering nearly all the Permian strata in the Tarim Basin. Zhang and Zou [2013], by analyzing chemical compositions of two magmatic dikes localities, argue for two distinct mantle domains in the Tarim Large Igneous Province: a long-term enriched continental lithospheric mantle of the Tarim domain in the south and a more depleted lithospheric mantle of the Central Asian Orogenic Belt (CAOB) region in the north (i.e., Tian Shan, Junggar and Altai), due to slab-derived fluids or subducted sediments. The existence of different lithospheric domains suggests different mantle compositions. In the Eastern Tibet, Song *et al.* [2007] analyze the mantle xenolith suites from North China Craton and Qaidam-Qilian Block. Their data suggest that the garnet peridotite massif from this zone is not a simple mantle fragment but a lithological association related to subduction zone magmatic processes before dragged down to deep mantle by the subducting oceanic/continental lithosphere. Ding *et al.* [2007] analyze mafic and ultramafic xenoliths from

**Table 1.** Major Elements Composition in the NCFMAS System for the Lithospheric Mantle and Asthenosphere Domains Used in the Modeling<sup>a</sup>

|                                | Mantle Compositions in the NCFMAS System (%)                 |   |  |   |  |
|--------------------------------|--|---|--|---|--|
|                                | Mantle 1 Lherz.<br>Average<br>[Griffin <i>et al.</i> , 2009] | Mantle 2—PUM Primitive<br>Upper Mantle [McDonough<br>and Sun, 1995] | Mantle 3 Lherz.<br>[El Messbahi<br><i>et al.</i> , 2015] | Mantle 4 Lherz.<br>[Cao and Zhu,<br>1987] | Mantle 5 Lherz.<br>[El Messbahi<br><i>et al.</i> , 2015] |
| SiO <sub>2</sub>               | 45.4   | 45  | 44.22  | 45.96                                     | 45.23  |
| Al <sub>2</sub> O <sub>3</sub> | 3.7  | 4.5   | 3.31   | 3.09                                      | 3.77   |
| FeO                            | 8.3  | 8.1   | 9.35   | 9.22                                      | 9.3  |
| MgO                            | 39.9   | 37.8  | 39.07  | 36.99                                     | 36.46  |
| CaO                            | 3.2  | 3.6   | 2.93   | 3.68                                      | 4.43   |
| Na <sub>2</sub> O              | 0.26   | 0.25  | 0.15   | 0.27                                      | 0.26   |
| Total                          | 100.76   | 99.25   | 99.03  | 99.21                                     | 99.45  |
| Mg#                            | 90.6   | 89.3  | 88.16  | 87.73                                     | 87.48  |

<sup>a</sup>Lherz. = Lherzolite.

central Qiangtang, but their petrological characteristics suggest that they were entrained from the lower crust or the crust-mantle transition boundary. Other crustal xenolith data from central Tibet have been published though they do not provide information on the mantle composition [Hacker *et al.*, 2000; Jolivet *et al.*, 2003; Chan *et al.*, 2009].

We tried to fit our results with the compositions derived from mantle xenolith data and found that these compositions are not suitable to explain all the geophysical observables (elevation, gravity, geoid, and seismic velocity anomalies). As explained in section 5 and in the supporting information, fitting the geophysical data along the A-B profile requires more fertile mantle compositions to allow increasing the mantle density and lowering the *P* wave mantle velocities. In consequence we referred to the age-classified lithospheric compositions by Griffin *et al.* [2003, 2009] and O'Reilly and Griffin [2006] and those compiled in global petrological databases (PetDB database, <http://www.earthchem.org/petdb>) to choose the optimal upper mantle oxides from real samples.

The selected lithospheric mantle compositions are detailed in Table 1. In agreement with the age of the last tectonothermal event [Artemieva, 2006], we consider a neo-Proterozoic lithospheric mantle for the Indian northern boundary (Mantle 1) [Griffin *et al.*, 2009]. The other lithospheric mantle compositions have been chosen to consistently fit all the observables with the geodynamic context (see also the supporting information). In order to analyze their effect on seismic velocities, we plot the depth variations of *P* wave velocity and density for the five lithospheric mantle compositions considered in this study, taking into account a thickness of 60 km and 200 km for the crust and lithosphere, respectively (Figure 4). These values correspond to the average structure of the India-Eurasia collision zone. Mantle 2 corresponds to the PUM from McDonough and Sun [1995]; Mantle 3 and Mantle 5 correspond to two lherzolites from El Messbahi *et al.* [2015]; and Mantle 4 corresponds to a lherzolite by Cao and Zhu [1987]. Fixing the mantle composition, the density within the lithospheric mantle depends on both temperature and pressure and, hence, on the lithospheric structure. The densest composition corresponds to Mantle 5 which is  $\sim 8 \text{ kg/m}^3$  denser than PUM (or Mantle 2). Mantle 5 is the only mantle composition which shows a decrease of the density of  $\sim 8 \text{ kg/m}^3$  at LAB depth. It is markedly denser than the other compositions, but it shows intermediate *P* wave seismic velocities. Mantle 1 composition, on the other hand, is the least dense mantle, but it is only  $\sim 0.01 \text{ km/s}$  slower than Mantle 2. Mantle 2 is the fastest composition, up to  $\sim 0.08 \text{ km/s}$  faster than Mantle 4,  $\sim 0.06 \text{ km/s}$  faster than Mantle 5, and  $\sim 0.03 \text{ km/s}$  faster than Mantle 3.

## 5. Results

The forward modeling scheme requires an initial model including the geometries of the crustal and lithospheric mantle bodies and their physical parameters. As a general procedure, we kept the initial crustal model (geometry and physical parameters) and we only modified it when strictly necessary to fit the surface observables, after trying different compositions and geometries for mantle bodies. Crustal modifications are always within the uncertainties associated with experimental data (principally from seismic data and geologic cross

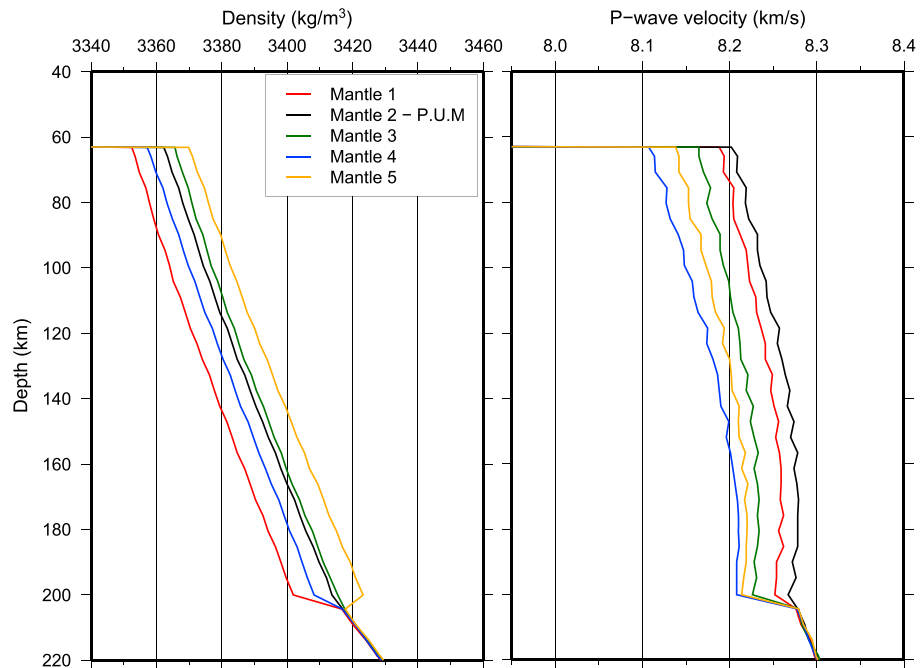


**Figure 4.** Density and *P* wave velocity variations on depth for each mantle composition, considering a flat model with parallel layers, where Moho depth is 60 km and LAB depth 200 km. Mantle compositions are detailed in Table 1.

sections). Note that the lines separating different mantle bodies are to be considered transition zones in which the mantle composition, i.e., the relative amount of the mantle minerals, varies *gradually* from one mantle body to the other, according to the pressure-temperature conditions.

The crust and lithospheric mantle structure of the *best fit model* are described in the following section. A selection of intermediate models is explained in the supporting information to illustrate the modeling procedure. In the supporting information we show results from *Model 0*, characterized by a 1-D mantle part (i.e., flat-LAB geometry and homogeneous lithospheric mantle composition), and a succession of progressively more complex models (*Models 1 to 4*). *Model 1* shows the effect of introducing lithospheric mantle thickness variations on the geophysical observables. *Models 2 to 4* show the effect of considering lateral variations in the lithospheric mantle composition. It is worth to notice that each intermediate model presented in the supporting information is the best fit of the trial-and-error procedure after some tens of runs each.

### 5.1. Crustal Structure

We build the crustal model using the information available from published data on the Himalayan-Tibetan region. The resulting crustal structure is shown in Figure 5, and the physical properties used for each crustal body are detailed in Table 2. Density and thermal conductivity values for crustal bodies have been derived from previous studies [e.g., Wang, 2001; Zhao *et al.*, 2003; Jiménez-Munt *et al.*, 2008; Bai *et al.*, 2013; Zhang *et al.*, 2014b]. Radiogenic heat production has been taken from a global compilation carried out by Vilà *et al.* [2010]. The average crustal density along our profile varies between 2825 kg/m<sup>3</sup> and 2870 kg/m<sup>3</sup>. Higher values (up to 2920 kg/m<sup>3</sup>) are modeled in the northern Qiangtang and Kunlun Shan due to the thick crust and the consequent high pressures in the lower crust. Our resulting crustal densities of the Himalayan foreland basin and Tibetan Plateau are consistent with the 3-D gravity modeling by Bai *et al.* [2013] and Zhang *et al.* [2014b]. They found average crustal densities of ~2800 kg/m<sup>3</sup> in the Himalayan foreland basin, increasing northward to ~2930 kg/m<sup>3</sup> in South Tibetan Plateau, where they modeled the thickest crust. Our average crustal density is 2830 kg/m<sup>3</sup> in the Tarim Basin, increasing northward to 2875 kg/m<sup>3</sup> in the CAO region. This northward increase is also modeled by Zhao *et al.* [2003] from ~2730 to 2850 kg/m<sup>3</sup> from the Tarim Basin to the Altai Range.

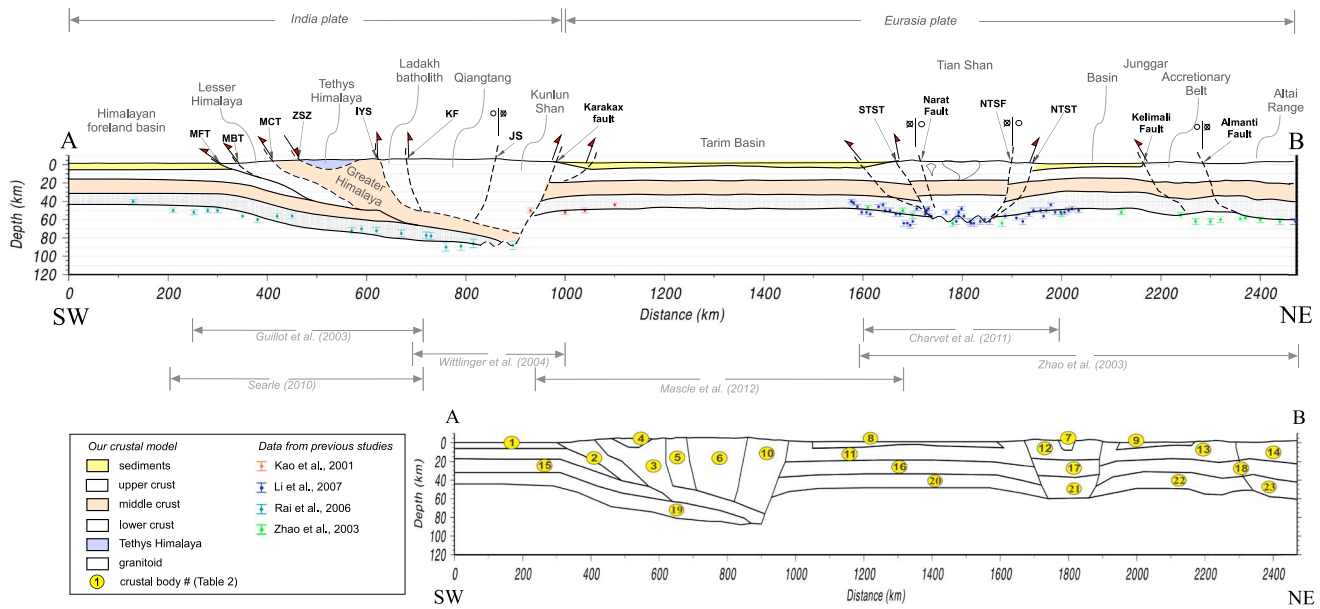


**Figure 5.** Crustal model of A-B profile. Physical properties of crustal bodies are reported in Table 2. IYS = Indus-Yarlung Suture; JS = Jinsha Suture; KF = Karakorum Fault; MCT = Main Central Thrust; MFT = Main Frontal Thrust; NTST = Northern Tian Shan Thrust; NTSF = Northern Tian Shan Fault; STST = Southern Tian Shan Thrust; and ZSZ = Zaskar Shear Zone.

The tectonic structure is based on the tectonic map by Yin and Harrison [2000] and on published geological cross sections [Guillot et al., 2003; Wang et al., 2003; Zhao et al., 2003; Wittlinger et al., 2004; Searle, 2010; Charvet et al., 2011]. The depth of the Moho discontinuity is constrained by several receiver function profiles [Kao et al., 2001; Zhao et al., 2003; Rai et al., 2006; Li et al., 2007] (and plotted on Figure 5) and by a wide-angle seismic profile to the north (CAOB region). The considered Moho geometry is also consistent with a number

**Table 2.** Physical Properties of the Different Tectonic Units Used in the Crustal Model Along A-B Profile<sup>a</sup>

| #  | Tectonic Units   | H ( $\mu\text{W}/\text{m}^3$ ) | K (W/K · m) | $\rho$ ( $\text{kg}/\text{m}^3$ ) | References for $\rho$                            |
|----|--|--------------------------------|-------------|-----------------------------------|--|
| 1  | Himalayan foreland basin                                 | $1.5 \exp(-z/15)$              | 2.3         | 2450–2487                         | Jiménez-Munt et al. [2008] and Bai et al. [2013] |
| 2  | India UC Lesser Himalaya                                 | $2.2 \exp(-z/15)$              | 2.5         | 2635–2725                         | Jiménez-Munt et al. [2008] and Bai et al. [2013] |
| 3  | Greater Himalaya   | $2 \exp(-z/15)$                | 2.5         | 2645–3240                         | Jiménez-Munt et al. [2008] and Bai et al. [2013] |
| 4  | Tethys Himalaya  | $1.2 \exp(-z/15)$              | 2.3         | 2650                              | Jiménez-Munt et al. [2008] and Bai et al. [2013] |
| 5  | Ladakh batholith   | $2 \exp(-z/15)$                | 2.3         | 2720–2800                         |  |
| 6  | Qiangtang  | $2 \exp(-z/15)$                | 2.4         | 2610–3050                         | Jiménez-Munt et al. [2008]                       |
| 7  | Granitoid  | 2                              | 2.5         | 2780                              | Zhao et al. [2003]                               |
| 8  | Tarim Basin sediments                                    | $1.2 \exp(-z/15)$              | 2.2         | 2590–2780                         |  |
| 9  | Junggar Basin sediments                                  | $1.2 \exp(-z/15)$              | 2           | 2600–2690                         | Zhao et al. [2003]                               |
| 10 | Kunlun Shan  | $2.2 \exp(-z/15)$              | 2.5         | 2620–3000                         |  |
| 11 | Tarim Basin UC   | $2 \exp(-z/15)$                | 2.5         | 2720–2790                         |  |
| 12 | Tian Shan UC   | $2 \exp(-z/15)$                | 2.3         | 2650–2725                         | Zhao et al. [2003]                               |
| 13 | Junggar (Basin and Accretionary Belt) UC                 | $2 \exp(-z/15)$                | 2.5         | 2720–2800                         | Zhao et al. [2003]                               |
| 14 | Altai Range UC   | $2 \exp(-z/15)$                | 2.2         | 2720–2790                         | Zhao et al. [2003]                               |
| 15 | India MC   | 0.3                            | 2.3         | 2910–2990                         | Bai et al. [2013]                                |
| 16 | Tarim Basin MC   | 0.3                            | 2.3         | 2800–2850                         |  |
| 17 | Tian Shan MC   | 0.3                            | 2.3         | 2850–2940                         | Zhao et al. [2003]                               |
| 18 | Altai Range and Junggar (Basin and Accretionary Belt) MC | 0.3                            | 2.3         | 2850–2950                         | Zhao et al. [2003]                               |
| 19 | India LC   | 2.1                            | 0.2         | 3000–3180                         | Bai et al. [2013]                                |
| 20 | Tarim Basin LC   | 2.1                            | 0.2         | 2990–3010                         |  |
| 21 | Tian Shan LC   | 2.1                            | 0.2         | 2950–3000                         | Zhao et al. [2003]                               |
| 22 | Junggar (Basin and Accretionary Belt) LC                 | 2.1                            | 0.2         | 3000                              | Zhao et al. [2003]                               |
| 23 | Altai Range LC   | 2.1                            | 0.2         | 3000                              | Zhao et al. [2003]                               |

<sup>a</sup>Depth-varying radiogenic heat production H (z is the depth in km); thermal conductivity K; and density  $\rho$  (the range is due to its depth dependence). UC: upper crust; MC: middle crust; and LC: lower crust.



of studies carried out in the Tarim Basin and Tian Shan, which depending on the methodology used (seismic tomography, receiver functions, surface wave dispersion, petrology, and gravity data) propose Moho depth values of 50–70 km below the Tian Shan and 40–50 km below the Tarim Basin [Belousov *et al.*, 1992; Kosarev *et al.*, 1993; Vinnik *et al.*, 2004; Shin *et al.*, 2007; Bagdassarov *et al.*, 2011; Steffen *et al.*, 2011, and references therein]. In our model the Moho depth below the Tian Shan is ~60 km and varies between 47 km and 57 km below the Tarim Basin. In the southern sector of the profile, the modeled Moho discontinuity is progressively deepening from the Indian plain northward, reaching the maximum depth (90 km) along the A-B profile below the Kunlun Shan. Our model shows a variable crustal thickness from the MCT to the JS, between 60 and 80 km, which is consistent with the ~70 km thick crust calculated in the Western Tibetan Plateau using the gravity data from the GOCE satellite mission [Tenze *et al.*, 2014]. The Himalayan orogen (Lesser Himalayan Sequence and Greater Himalayan Sequence) and the Western Tibetan Plateau overthrust the lower Indian crust until the Jinsha Suture (~600 km) (Figure 5). Both of them lay on top of the Indian middle-lower crust and are separated from the Tarim Basin by the north verging Kunlun Shan. The Tarim Basin is mostly characterized by gently deformed strata, underthrust below the southern Tian Shan. The thickness of the sedimentary cover in the Tarim Basin is not completely homogeneous, thrust over the two borders by the Tian Shan in the north and the Kunlun Shan in the southwest, respectively [Masclé *et al.*, 2012]. Farther north, the Junggar Basin is characterized by a similar tectonic structure, with the crustal layers dipping to the south beneath the northern Tian Shan.

## 5.2. Upper Mantle Structure

Figure 6 shows the best fit model obtained by considering lateral variations of the lithospheric mantle thickness and composition. According to tomography, we have also considered a thermal anomaly ( $\Delta T = 60^\circ\text{C}$ ) in the sublithospheric domain beneath the Tarim Basin. This sublithospheric thermal anomaly is assumed coupled to the lithosphere in calculating the elevation due to its large wavelength ( $>800$  km), which facilitates the transmission of vertical stresses (for more details see section 3 and Carballo *et al.* [2015b]). However, this is a matter of debate since coupling/decoupling depends on the viscosity profiles of the mantle and, especially, of the crust, but the methodology we used does not consider rheological parameters. Four different mantle bodies with different compositions are used to satisfy all the geophysical data considered in our approach, although they do not aim to represent the “true” mantle composition along the selected profile (see Table 1 and supporting information for details). A complete analysis of chemical compositions and resulting physical properties has been performed by Afonso *et al.* [2013a, 2013b] showing that more than one composition can result in the same densities and velocities at given P-T conditions. Therefore, the lithospheric mantle compositions cannot be resolved univocally from our modeling. We can only show mantle compositions compatible with geophysical observations and petrological data, providing information on enrichment/depletion in major elements playing a key role on the density and seismic velocity distributions within the lithospheric mantle.

The calculated surface heat flow, ranging between 40 and 60 mW/m<sup>2</sup>, is not so well constrained owing to its scarcity and associated uncertainty, particularly in the south of the profile (Figure 6). However, the results are consistent with the heat flow values from Wang [2001] and An and Shi [2007] illustrated in section 4.1. The resulting elevation, gravity, and geoid anomalies match the major observed trends along the profile. Local misfits in the Bouguer anomaly (15–20 mGal) are noticed at the southern edge of the Tarim Basin, probably related to local crustal features not considered in our model. The two frontal regions of the Tian Shan also show misfits in the elevation (400–600 m), though noticeably lesser than in previous models (see supporting information). These discrepancies can be explained by flexural effects related to regional isostasy as these regions are characterized by elastic thicknesses larger than 40 km [Braitenberg *et al.*, 2003; B. Chen *et al.*, 2015]. Liu *et al.* [2004] also point out that flexural deformation characterizes the northern margin of the Tarim Basin, since the rigidity of the basin transfers the strain originating from the far-field India-Eurasia collisional stresses toward the north, releasing it into flexure under the sedimentation and tectonic loading associated with uplift in the Tian Shan.

From south to north, the resulting LAB depth varies from 220 km below the Himalayan foreland basin to 295 km below the Kunlun Shan, decreasing to ~240 km below the Tarim Basin and to ~260 km below the Tian Shan (Figure 6e). Farther north, the base of the lithosphere progressively deepens from ~260 km depth below the Junggar region to ~280 km underneath the Altai Range.

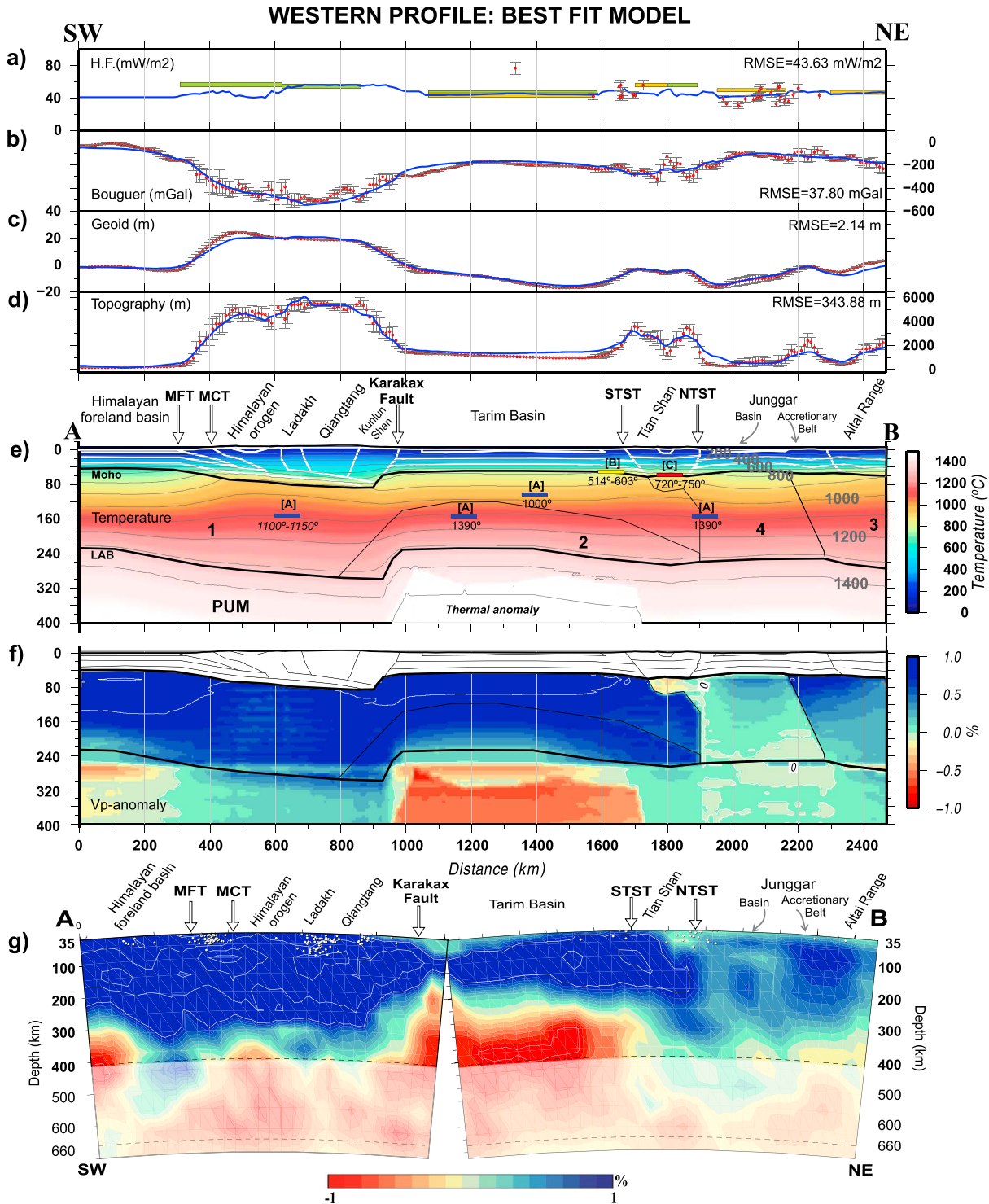


**Figure 6.** A-B profile, best fit model. (a) Surface heat flow; orange and green horizontal bars in the heat-flow panel are mean heat flow values from Wang [2001] and An and Shi [2007], respectively. (b) Bouguer gravity anomaly. (c) Geoid height. (d) Topography. Blue lines represent the calculated values from the model. Red dots denote measured data, and vertical bars denote the standard deviation calculated on a strip of 50 km width (500 km for surface heat flow). (e) Temperature distribution, numbers 1–4 and PUM indicate the chemical composition (Table 1). Thick horizontal bars in the temperature panel are temperatures from different studies ([A] An and Shi, 2007; [B] Liu et al., 2004; [C] Bagdassarov et al., 2011). (f) P waves velocity anomalies, relative to the column located at 1910 km distance along the profile (see details on the text). (g) P wave seismic tomography model (described in section 4.3). MCT = Main Central Thrust; MFT = Main Frontal Thrust; NTST = Northern Tian Shan Thrust; and STST = Southern Tian Shan Thrust.

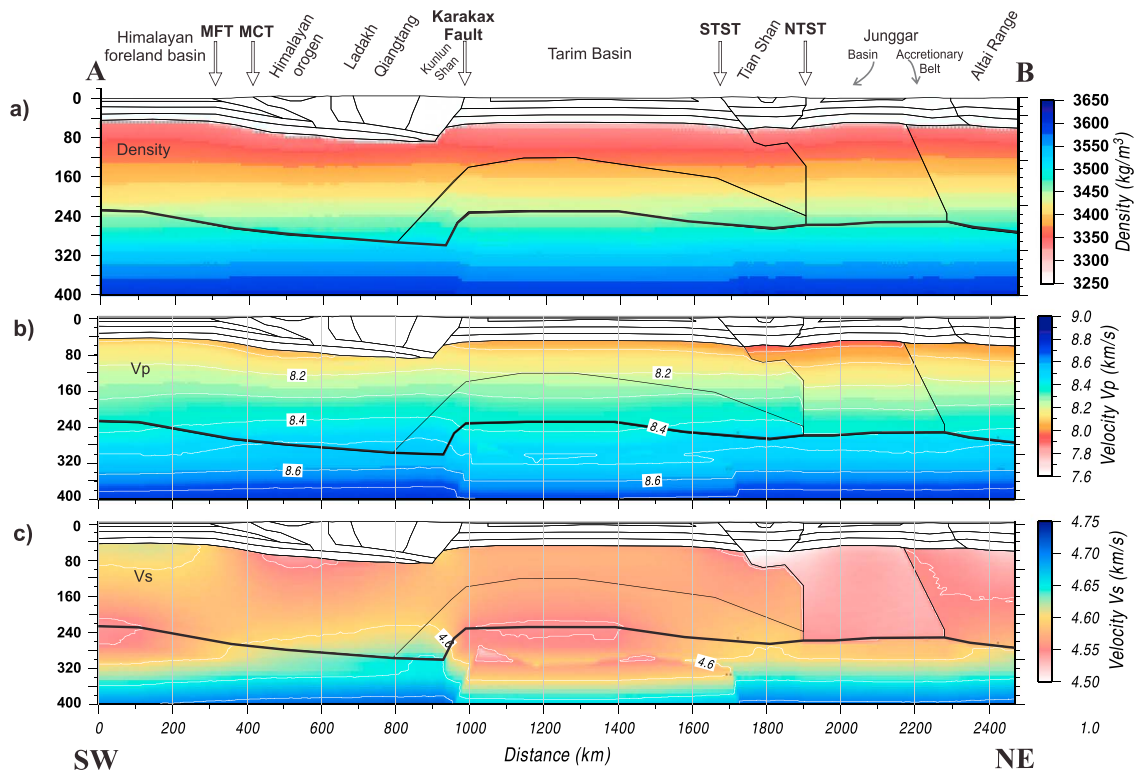


**Figure 7.** Calculated mantle density and  $P$  wave and  $S$  wave seismic velocities along A-B profile, in the best fit model.

The temperature distribution along the profile (Figure 6e) shows upward deflections of the isotherms according to the increase of crustal thickness and the consequent higher radiogenic heat production, especially accentuated beneath the Western Tibetan Plateau, Tian Shan, and the Junggar Accretionary Belt. The Moho temperature is  $\sim 650^{\circ}\text{C}$  in the Himalayan foreland basin and Tarim Basin,  $800^{\circ}\text{C}$  in the Junggar Basin, and  $\sim 900^{\circ}\text{C}$  in the Himalayan-Tibetan Plateau region, Tian Shan, Junggar Accretionary Belt, and Altai Range. The maximum temperature at Moho discontinuity is just over  $900^{\circ}\text{C}$  below the Kunlun Shan. The Moho temperatures in Tarim and Tian Shan regions are in agreement with values obtained by field-based geothermal analysis and thermal-petrology studies [Liu *et al.*, 2004; Bagdassarov *et al.*, 2011]. Lower crust temperatures exceeding  $800^{\circ}\text{C}$  in Tibet are consistent with the presence of granulite/eclogite facies metamorphism [Groppo *et al.*, 2007; Grujic *et al.*, 2011; Warren *et al.*, 2011]. Our modeled mantle temperatures match the temperatures estimated from seismic tomography in the western Himalayan-Tibetan region and central Tarim [An and Shi, 2007] and disagree in south Tarim Basin and Tian Shan, where these authors predicted higher values ( $\sim 1390^{\circ}\text{C}$  at 150 km depth). An and Shi [2006] published a seismic-thermal lithosphere map where the LAB is located at 140–170 km depth beneath the Tarim Basin and Tian Shan. These depths are considerably shallower than those predicted in our model (230–250 km) and the 250 km in the Tarim Basin proposed by Wang [2001].

The lithospheric mantle density (Figure 7a) increases from the Moho to the bottom of the lithosphere from  $3350\text{ kg/m}^3$  to  $3500\text{ kg/m}^3$ , with the maximum values at the LAB depth below the Kunlun Shan. At the same temperature-pressure conditions, lateral variations up to  $\sim 50\text{ kg/m}^3$  can be noticed due to compositional changes (different mantle bodies). Below the LAB, the sublithospheric mantle density increases continuously until values of  $3600\text{ kg/m}^3$ , due to the predominant effect of pressure. The sublithospheric thermal anomaly of  $60^{\circ}\text{C}$  beneath the Tarim Basin results in a mantle density decrease of  $\sim 10\text{ kg/m}^3$ .

Seismic velocities within the lithospheric mantle range from  $7.9\text{ km/s}$  to  $8.50\text{ km/s}$  and from  $4.5\text{ km/s}$  to  $4.65\text{ km/s}$  for  $P$  and  $S$  waves, respectively (Figures 7b and 7c). In both cases, maximum values characterize the deepest lithospheric mantle below the Kunlun Shan, near the base of the lithosphere, while minimum  $V_p$  and  $V_s$  values are found at Moho depths below the Junggar Basin and the Tian Shan, respectively. In

the sublithospheric domain,  $P$  and  $S$  wave seismic velocities increase progressively with depth to values of  $\sim 8.75$  km/s and  $\sim 4.7$  km/s at 400 km depth, respectively. Beneath the Tarim Basin these values are slightly lower ( $\sim 1\%$ ) due to the considered sublithospheric thermal anomaly.

The velocity anomalies are calculated assuming a 1-D reference velocity model. Global seismic tomography commonly uses the AK135 reference model [Kennett *et al.*, 1995], which represents a global average of seismic velocities corresponding to a simple stratified Earth with 35 km thick crust and 120 km thick lithospheric mantle. The thick crust of the India-Eurasia collisional system (up to 90 km thick in the Western Tibetan Plateau) [Rai *et al.*, 2006; Zhao *et al.*, 2010] makes the AK135 unsuitable for a realistic analysis of the upper mantle anomalies in the region, especially at lithosphere levels. Therefore, we opted for calculating the mantle seismic velocity anomalies relative to a reference column selected along the modeled profile. The column that shows nearly null anomaly in the tomography image (Figures 3a and 6g) will be our reference column. In this way, our modeled seismic anomalies and the tomographic ones will have the same zero level, and this will permit to compare the lateral variations of the  $P$  wave anomaly along the profile between our model and the seismic tomography. Our reference column is selected just north to the Northern Tian Shan Thrust (NTST) at 1910 km distance from the beginning of the profile (Figure 6f).

The localization of the largest modeled positive anomalies ( $\geq 1\%$ ) below the Himalayan foreland basin, Himalaya-Tibet Plateau, and Tarim Basin (Figure 6f) is consistent with the seismic tomography image (Figure 6g). The compositional changes below the Junggar and Altai regions allow explaining the reduced amplitude of the seismic velocity anomaly in the northern half profile with respect to the southern part. Beneath the Tarim Basin, the positive  $V_p$  anomaly goes down to  $\sim 200$  km and a low velocity zone in the sublithospheric domain below 300 km depth, results from the predefined thermal anomaly.

## 6. Discussion

### 6.1. India-Eurasia Collision Along the Western Profile

We calculated the root-mean-square error (RMSE) and the deviations along the profile for the gravity anomaly, geoid, and elevation, and we compare the obtained values between the different presented models including the best fit model and Models 0 to 4 (Figures 6, A1 to A5 in the supporting information, and Figure 8). With respect to the initial model Model 0, the best fit model allows reducing the RMSE errors by 22%, 36%, and 21% for the gravity anomaly, geoid height, and elevation, respectively (Figure 8a). This means that the deviations have been reduced by 20–40 mGal for the gravity, 2–6 m for the geoid height and 200–500 m for the topography, depending on the position along the profile (Figure 8b). The  $P$  wave seismic tomography is not included in the RMSE calculations; however, from Figures 6 and A1 to A5 we can conclude that our best fit model displays the best adjustment.

The southern sector of the western profile shows a lithospheric thickness similar to the results obtained by Zhao *et al.* [2010] using receiver functions technique along their western line (west line). Their results show a lithosphere thickening from 130 km below the Indian foreland to 200 km beneath the west Tibet. The lithosphere thickness decreases abruptly to  $\sim 140$  km below the Tarim Basin. However, all Zhao *et al.* [2010] values are nearly 100 km thinner than ours. The systematic lower values between the seismic LAB relative and the thermal LAB have been pointed out by other studies showing the strong dependence of these results on the observation method [Eaton *et al.*, 2009; Yuan and Romanowicz, 2010; Tunini *et al.*, 2015].

Our results show that the lithospheric mantle from the foreland basin to the Tibetan Plateau is characterized by a high positive  $V_p$  anomaly (up to 2%, Figure 6f) penetrating down to  $\sim 300$  km. However, in the Tarim Basin the positive anomaly reaches just 200 km depth, with negative values below 260 km. This  $P$  wave anomaly distribution is in agreement with the work by Huang and Zhao [2006]. At 200 km depth, the calculated  $V_s$  (Figure 7c) shows higher values beneath the Tibetan Plateau than below the Tarim Basin, a feature also imaged by Li *et al.* [2008] and Feng and An [2010]. The seismically fast lithospheric mantle in the southern half of the profile can be interpreted as the northward subduction of the Indian plate, as pointed out from published tomography studies [e.g., Tilmann *et al.*, 2003; Wittlinger *et al.*, 2004; Li *et al.*, 2008]. Similarly, the step-like topography of the LAB, with a sharp jump of  $\sim 70$  km below the Karakax Fault, is interpreted as the northern boundary of the Indian plate, as suggested by Zhao *et al.* [2010].



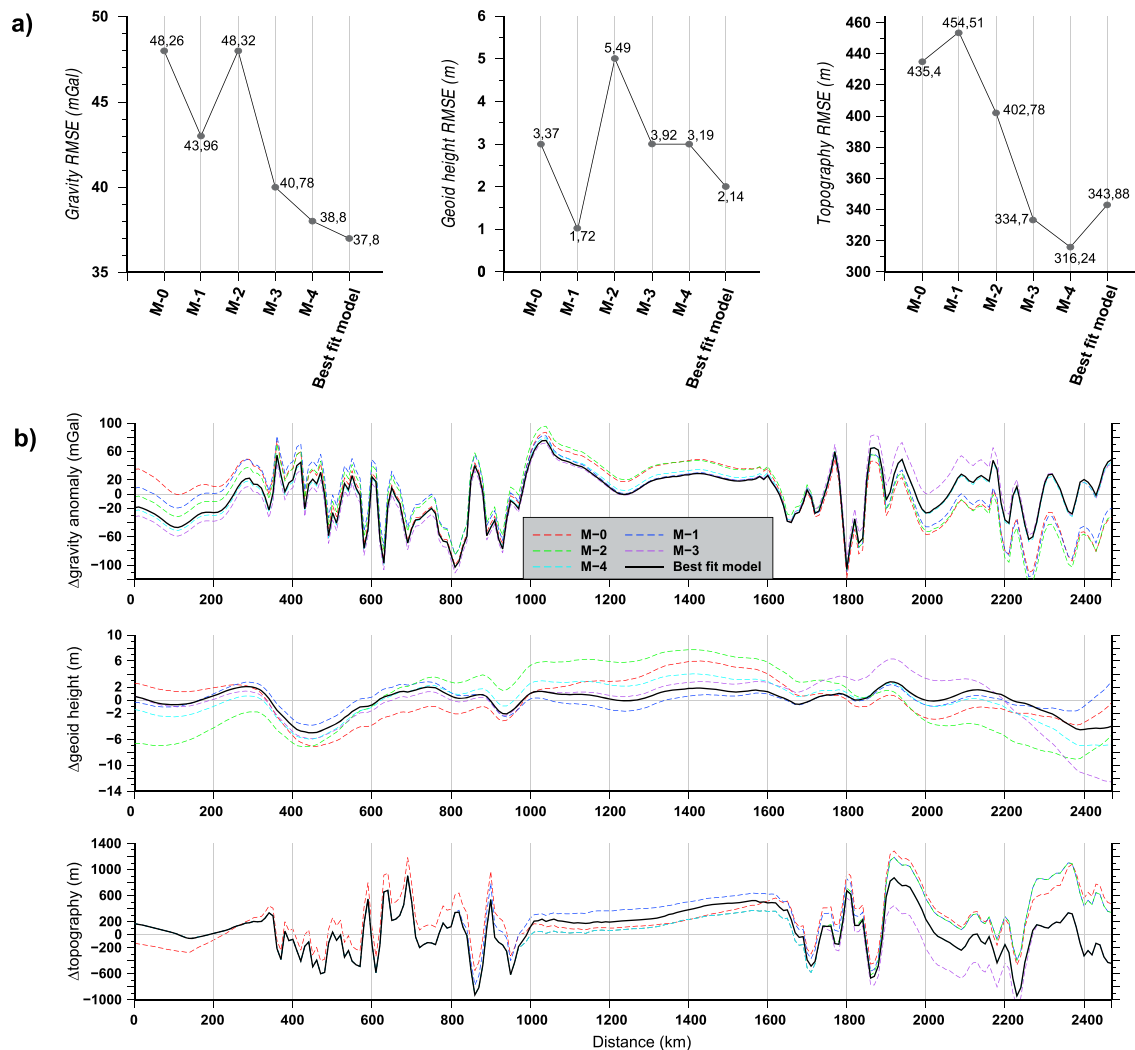


**Figure 8.** Score of all models performed in the western Profile A-B, from Model 0 to Model 4, (in supporting information) and the best fit model (Figure 6). (a) Root-mean-square errors (RMSEs) for gravity anomaly, geoid height, and topography. (b) Deviations along the profile of gravity anomaly, geoid height, and topography.

The NE thickening of the Tarim lithosphere toward the Tian Shan (Figure 6f) is in agreement with the *P* wave tomography study by Xu *et al.* [2002]. These authors estimate that the lithosphere of the central and northern Tarim Basin is thicker (>200 km LAB depth) relative to the southern Tarim Basin and Junggar region (170–180 km). Teleseismic *P* wave tomography imaged a ~2% slower lithospheric mantle beneath the Tian Shan relative to the Tarim Basin [Lei and Zhao, 2007]. Similar results have also been found for *P* and *S* wave velocities [Lei, 2011]. Furthermore, our low *V<sub>s</sub>* values (4.2–4.4 km/s) in the Tian Shan are consistent with values derived by Vinnik *et al.* [2004] using receiver function tomography in the western Tian Shan. From Figures 6f and 6g, we can interpret that the seismically faster Tarim lithospheric mantle is plunging below the slower Tian Shan mantle, a feature also observed by Poupinet *et al.* [2002] from *P* wave tomography and by Zhao *et al.* [2003] from magnetotelluric surveys.

Seismic tomography (Figure 6g) shows that the Junggar Basin is characterized by average *V<sub>p</sub>* values in the lithospheric mantle lower than below the Tian Shan and Altai Range. We modeled this velocity change as compositional origin, which could be related to either refertilization acting in the subcontinental lithospheric mantle, due to the circulation of melts (Lherz Massif) [e.g., Le Roux *et al.*, 2007] or metasomatic events as frequently reported for mantle xenoliths sampled in cratonic areas [e.g., Pearson *et al.*, 1995; Griffin *et al.*, 2000; Bell *et al.*, 2005]. Alternatively, low *V<sub>p</sub>* values could be explained by thermal processes related to upwelling of hot material, as suggested for the central and western Tian Shan by different seismic studies [Vinnik *et al.*, 2004;

Kumar *et al.*, 2005; Lei and Zhao, 2007; Lei, 2011]. In this case, however, fitting the observables would require unrealistic high crustal densities.

Below the CAO region there is a noticeable discrepancy between our thermal LAB and the LAB depth inferred by Zhao *et al.* [2003] using the magnetotelluric sounding. These authors claim for a lithospheric thickness of ~130 km below the Junggar Basin and ~160 km beneath the Tian Shan and Altai Range, providing evidences for the presence of conductive layers in the crust and upper mantle of the Tian Shan, and a high resistive Tarim plate subducting into the upper mantle below. The resulting lithosphere thickness from our best fit model is ~100 km thicker below the ranges (Tian Shan and Altai) and ~120 km thicker below the Junggar Basin. These discrepancies are related to the different methodologies used to image the lithosphere-asthenosphere boundary, but the relative thickness variations are similar.

A negative  $V_p$  anomaly (~–1%) can be interpreted as caused by either a positive thermal anomaly or by a change in composition. In our model, we consider that the seismically slow sublithospheric mantle beneath the Tarim Basin has a thermal origin ( $\Delta T = 60^\circ\text{C}$ ), which becomes in a density variation of ~–10 kg/m<sup>3</sup>. The origin of this thermal anomaly would be related to sublithospheric mantle flow. Alternatively, a chemical origin of such  $P$  wave tomography anomaly would require a composition similar to the lithospheric mantle beneath the Junggar region (Mantle 4), which would result in a  $V_p$  anomaly of ~–1% and a density anomaly of ~–6 kg/m<sup>3</sup> under the condition of thermal equilibrium ( $\Delta T = 0^\circ\text{C}$ ). The origin of such compositional anomaly could be related to some mantle detachment occurred long time ago to reach the thermal equilibrium with the surrounding sublithospheric mantle but keeping the original composition at those depths. Although not conclusively, we prefer the thermal interpretation since chemical anomalies convey density anomalies and sublithospheric mantle flow, which in turn modifies the thermal regime. It is worth noting, however, that the fit of the geophysical observables and the resulting lithospheric geometry is not modified significantly.

Four lithospheric mantle domains have been defined according to their different chemical compositions, seismic velocities, and thicknesses (Figure 6): (1) the subducting Indian lithospheric mantle (Mantle 1) underlying the Himalayan orogen, Tibetan Plateau, and Kunlun Shan reaching lithospheric mantle thicknesses of ~210 km and separated from the Eurasian lithospheric mantle by a jump in both LAB and Moho discontinuities, coinciding with the Karakax fault; (2) the Tarim (Eurasian) lithospheric mantle domain (Mantle 1) plunging northward below the Tian Shan, with its deepest portion (Mantle 2) fertilized, with a thickness of about 180 km and underlined by a thermal sublithospheric anomaly (below 300 km depth); (3) the Junggar mantle (Mantle 4) characterized by low velocity and ~195 km thick; and (4) the northern lithospheric mantle domain beneath the Altai Range.

## 6.2. India-Eurasia Collision Along the Eastern Profile

Numerous studies [Kumar *et al.*, 2006; Jiménez-Munt and Platt, 2006; Jiménez-Munt *et al.*, 2008; Zhao *et al.*, 2010; Ceylan *et al.*, 2012; Guillot and Replumaz, 2013] suggest the occurrence of a lithospheric mantle thinning beneath the northeastern Tibetan Plateau, with the LAB located at 100–170 km beneath the north Lhasa and Qiangtang terrains. This thinning would explain the low  $P$ ,  $P_n$ , and  $S$ ,  $S_n$  wave velocity anomalies and the low Rayleigh wave phase velocities observed in the region, which combined with the high electrical conductivities suggest a hot environment throughout the crust and upper mantle [Yue *et al.*, 2012, and references therein]. The 2-D lithospheric thermal and density models, presented by Jiménez-Munt *et al.* [2008], along the C-D transect (Figure 1 for location) agree with this hypothesis, proving the need of a thin and hot lithosphere to explain the high topography, gravity, geoid, and crustal temperatures of the northeastern plateau. The seismic tomography model (Figure 9g) obtained using the method described in section 4.3 images strong positive anomalies (up to 4%) from the Himalayan foreland basin northward, till the Indus-Yarlung Suture. North of the suture, a slightly positive (~0.2–0.4%)  $V_p$  anomaly is imaged between 100 and 250 km depth below the Lhasa terrain, whereas a slightly negative (~–0.4%) anomaly is imaged between 150 and 250 km depth below the Qiangtang and Songpan-Ganzi terrains and between 250 km and 400 km depth below the Qaidam Basin. This low-velocity anomaly has been largely interpreted as due to localized upwelling of asthenospheric material above the subducting slab [DeCelles *et al.*, 2002; Tilmann *et al.*, 2003; Ren and Shen, 2008; Liang *et al.*, 2011, 2012]. However, the location and spatial extent of this upwelling zone remains controversial. DeCelles *et al.* [2002] and Ceylan *et al.* [2012] locate the low velocity zone north of the Bangong Nujiang Suture, but the recent receiver function study by Shi *et al.* [2015] places the mantle

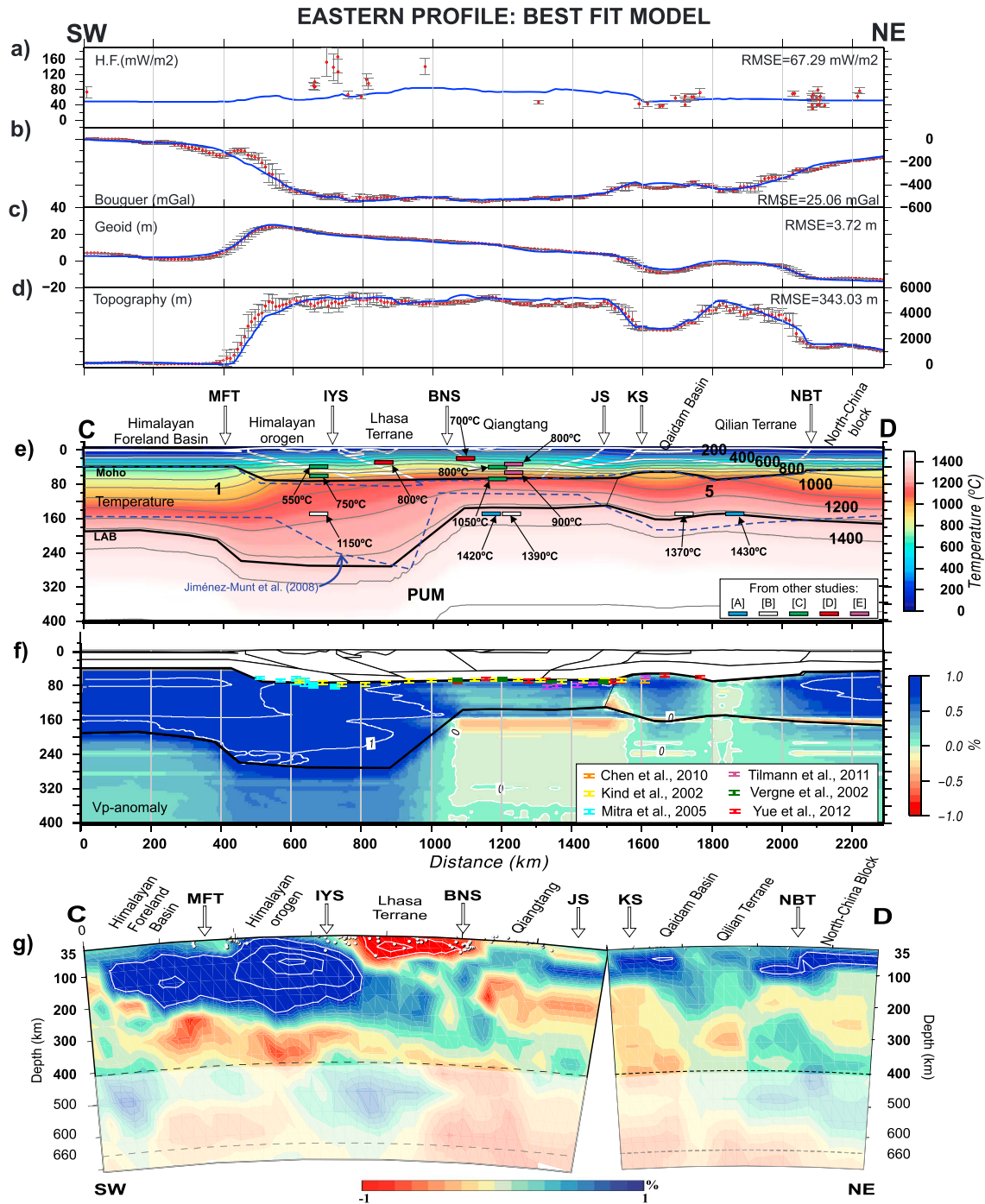


**Figure 9.** C-D profile, best fit model. (a) Surface heat flow, (b) Bouguer gravity anomaly, (c) geoid height, and (d) topography. Blue lines represent the calculated values from the model. Red dots represent the data measured data, and vertical dispersion bars denote the standard deviation calculated on a strip of 50 km width (500 km for surface heat flow). (e) Temperature distribution, numbers (1, 5) and PUM indicate the chemical composition (Table 1). Thick horizontal bars are temperatures taken from [A] Priestley and McKenzie [2006], [B] An and Shi [2007], [C] Galvé et al. [2006], [D] Mechie et al. [2004], and [E] Hacker et al. [2000]. (f) P waves velocity anomalies relative to the column located at 1800 km distance along the profile (see details on the text). (g) P wave seismic tomography model (described in section 4.3). BNS = Bangong Nujiang Suture; IYS = Indus- Yarlung Suture; JS = Jinsha Suture; KS = Kunlun Suture; MFT = Main Frontal Thrust; and NBT = North Border Thrust.

wedge south of the BNS and then below southern Lhasa (south of 31°N). The Qaidam Basin and the North China block are characterized by a seismically fast upper mantle (up to 1%  $V_p$  anomaly), especially in the first 200 km depth.

We have remodeled this profile using the same approach used for A-B transect to investigate the relative importance of the mantle chemical composition on the density and seismic velocities and therefore on the resulting lithospheric structure (Figure 9). In the next paragraphs we present our results along the C-D profile, and in the next section we discuss the differences between the western and eastern sectors of the Tibetan Plateau. The supporting information includes the intermediate models along the C-D profile to reach the best fit model.

The best fit model along the C-D profile (Figure 9) considers the same crustal structure provided by *Jiménez-Munt et al.* [2008]. Only small differences in the Moho depth have been incorporated to update the crustal thickness values used by *Jiménez-Munt et al.* [2008] with the most recent data [Yue et al., 2012; Zhang et al., 2011]. As we already discuss in section 4.4, there is one locality in the Eastern Tibet (in Qaidam-Qilian Block) where mantle xenolith suites have been analyzed [Song et al., 2007]. Unfortunately, they were not suitable to explain the observables, in particular the lower lithospheric mantle velocity beneath the Qaidam-Qilian zone relative to the Indian-Himalayan-South Tibetan Plateau. Therefore, as with the western profile, we had to refer to the PetDB xenolith global database to look for a composition able to reproduce the mantle seismic velocities. We consider a mantle composition beneath the Qaidam, Qilian, and North China block slightly more fertile relative to that of the Himalayan-Tibetan Plateau region (Figure 9e).

A fertile Mantle 5 composition (Table 1) allows reducing about 8% the  $P$  wave velocity in the lithospheric mantle, generating  $V_p$  anomalies about 2% smaller below the Qaidam and North China block than below the Himalayan orogen and foreland basin. However, the higher content in FeO, CaO, and also moderately in  $Al_2O_3$  with respect to Mantle 1 increases the mean density of the lithospheric mantle. In consequence, we have reduced the LAB depth by ~50 km to keep the fit with the density-dependent observables (elevation, gravity, and geoid). The resulting lithospheric model (Figure 9) is therefore characterized by a thick and dense lithospheric mantle below the Himalayan orogen and southern sector of the Tibetan Plateau (~250 km) and a thinner lithospheric mantle (140–170 km) below the Qiangtang, Sonpan-Ganze, Qaidam, Qilian, and North China regions.

This model confirms the results obtained by the thermal modeling by *Jiménez-Munt et al.* [2008], though the LAB topography is slightly different. The newly modeled Indian lithospheric mantle is up to 100 km thicker beneath the Himalayan orogen and ~40 km beneath the Qiangtang terrain. A lithospheric root is shown below the Qaidam Basin, with the LAB located at ~160 km depth (~20 km less than in *Jiménez-Munt et al.* [2008]). Farther north, our LAB descends from the Qilian Shan, in contrast to *Jiménez-Munt et al.* [2008] who propose a LAB shallowing ~40 km along this section of the profile.

The pronounced lithospheric thinning beneath the eastern Qiangtang is consistent with the available geothermobarometry data (Figure 9) showing very high temperatures at middle lower crustal levels (800–1050°C at 40–70 km depth) [Galvé et al., 2006; Hacker et al., 2000] and at upper sublithospheric levels (1390–1420°C at 140 km depth) [Priestley and McKenzie, 2006; An and Shi, 2007] as extensively discussed in *Jiménez-Munt et al.* [2008]. Note that considering just a chemical anomaly (i.e., no mantle thinning) would reduce the calculated temperatures by about 200°C at these depths (see previous models for the Eastern profile in the supporting information). Moreover, in order to keep the fitting with observables the new composition should be such that reduces the  $V_p$  by about 0.5% relative to PUM at about 1200°C but has a similar density than PUM at about 1400°C at depths of 160–180 km. None of the selected and tested mantle compositions from PetDB petrological database fit these conditions and other mantle composition would pose difficulties in justifying its origin.

Along this eastern profile we can differentiate only three lithospheric mantle domains according to their variable chemical compositions, seismic velocities, and thicknesses (Figure 9): (1) the Indian lithospheric mantle underlying the eastern Himalayan orogen and the Lhasa terrain up to the Bangong-Nujiang Suture and characterized by Mantle 1 composition and a great thickness exceeding 200 km; (2) the lithospheric mantle beneath the Qiangtang with Mantle 1 composition and only 70 km thick; and (3) the Eurasian lithospheric mantle below the Qaidam Basin, Qilian Shan, and North China Block of Mantle 5 composition and thicknesses of about 120 km and variable LAB topography. This triple partition of the lithospheric mantle along the eastern transect follows the results of the receiver function study by Zhao et al. [2010], in which the transitional lithospheric region is defined as the “crush zone,” sandwiched between the India and the Eurasia plate.



**Table 3.** The RMSE<sup>a</sup> Between Measurements and Calculated Data (See Explanations in the Text)

|   | Bouguer anomaly (mGal) | Geoid (m) | Topography (m) |
|---|------------------------|-----------|----------------|
| <i>Profile A-B</i>                                      |                        |           |                |
| Model 0   | 48.26                  | 3.37      | 435.4          |
| Model 1   | 43.96                  | 1.72      | 454.51         |
| Model 2   | 48.32                  | 5.49      | 402.78         |
| Model 3   | 40.78                  | 3.92      | 334.70         |
| Model 4   | 38.80                  | 3.19      | 316.24         |
| Western best fit model                                  | 37.80                  | 2.14      | 343.88         |
| <i>Profile C-D</i>                                      |                        |           |                |
| Model 0-E   | 39.32                  | 8.59      | 335.20         |
| Model 1-E   | 25.04                  | 3.86      | 335.42         |
| Eastern best fit model                                  | 25.06                  | 3.72      | 343.03         |
| Model with compositions from <i>Vozar et al. [2014]</i> | 33.9                   | 6.17      | 642.58         |

<sup>a</sup>RMSE =  $\frac{1}{N} \left( \sum_{i=1}^N (x_{(i)obs} - x_{(i)calc})^2 \right)^{1/2}$ , where  $x_{obs}$  and  $x_{calc}$  are the observed and calculated data, respectively, and  $N$  is the number of total points along the profile depending on the horizontal discretization. In this study,  $N$  is 249 and 230 for A-B and C-D profile, respectively.

The recent geophysical-petrological study of central Tibet by *Vozar et al. [2014]* also shows a lithosphere thinning beneath the Qiangtang terrain but with a more moderate jump in the LAB depth below Lhasa terrane (60–80 km, with respect to 120 km in our model). Their petrological results are consistent with the presence of a compositional variation under the Tibetan Plateau, suggesting a fertile garnet-lherzolite lithospheric mantle below the Qiangtang, and a Fe-rich spinel-harzburgite lithospheric mantle below Lhasa. We tested the compositions of *Vozar et al. [2014]* along our profile for the Qiangtang (garnet-lherzolite) and the India lithospheric mantle (Fe-rich spinel-harzburgite), but the results show that the RMSE between calculated and observed data is twice than our model (Table 3). The increased amount of Fe in the India lithosphere results into a strong decrease of the elevation in the southern Tibetan Plateau and further misfits in the geoid anomaly. A shallower LAB could overcome the difficulties, but it would produce a decrease in the positive seismic anomaly below the southern Tibetan Plateau, which works against seismic tomography results.

### 6.3. Lithospheric Structure Variations in the India-Eurasia Collision Zone and Geodynamic Implications

Our lithospheric models help to refine the deep structure of the India and Eurasia collisional orogen both in cross section (western and eastern transects) and along its strike. The modeled profiles delineate the present position of the northern edge of the Indian lithospheric mantle beneath the thrust system of the Himalaya and Tibetan Plateau and suggest decoupling and strain partitioning between the crust and the lithospheric mantle. Finally, the integration of the modeled lithospheric profiles with seismic tomographic images allows interpreting the structure of the Indian lithosphere subducting beneath Eurasia.

The variations of lithospheric mantle compositions determined in this study are consistent with the distribution of the large-scale tectonic domains made of continental blocks or terrains separated by suture zones (Figure 1). According to our results, the Indian lithospheric mantle is characterized by a homogenous chemical composition (Mantle 1) in both western and eastern sides of the Tibetan Plateau (Profiles A-B and C-D, respectively, Figure 10). On the contrary, the Eurasian lithospheric mantle shows a higher compositional variability, with different lithospheric mantle domains reflecting the different amalgamated blocks caused by the closing of different branches of the Tethys Ocean [e.g., *Pubellier et al., 2008; Replumaz and Tapponnier, 2003; van Hinsbergen et al., 2011, 2012*] (Figure 10). Our models show that the extent of the thick Indian lithospheric mantle (Mantle 1) beneath the Himalayan orogen and Tibetan Plateau is of ~630 km to the north of the Main Frontal Thrust in the western profile (Figure 6) and ~550 km along the eastern profile (Figure 9). This shorter length of the Indian lithospheric mantle in the eastern profile contrasts with the eastward increasing width of the Tibetan Plateau varying from ~600 km to 1100 km. In addition, this shorter length in the eastern profile makes the northern limit of the well-characterized Indian lithospheric mantle crossing the Qiangtang tectonic domain slightly oblique to its tectonic shape (Figure 10): to the West, the Indian plate underthrusts the whole Tibetan Plateau up to the Karakax Fault, whereas to the East, it underthrusts only the southern half of the plateau (up to the Bangong-Nujiang Suture, BNS in Figure 10). The

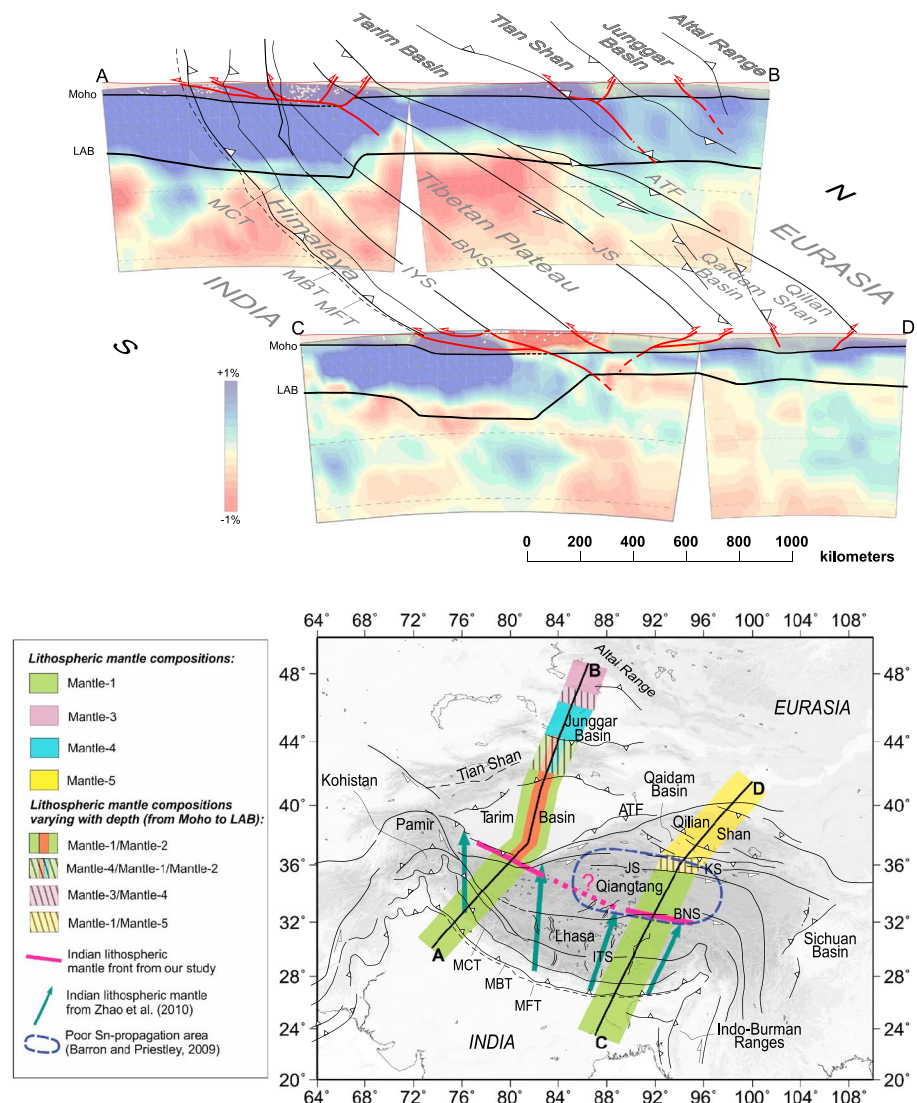


**Figure 10.** (a) Along-strike comparison of the resulting crustal and lithospheric mantle structures of the two modeled profiles, superimposed to the seismic tomography. (b) Resulting mantle compositions and localization of the northern edge of the Indian mantle lithosphere.

obtained position of the northern boundary of the Indian lithospheric mantle is in agreement with results from receiver functions by Zhao *et al.* [2010] and the analysis of *P* wave shallow tomography sections by Li *et al.* [2008] and Replumaz *et al.* [2013].

The lithospheric mantle composition corresponding to Mantle 1 is also present beneath both, the Tarim Basin to the west the Qiangtang and the Songpan-Ganzi domains to the east, although a more fertile Mantle 2 PUM is needed along the entire lowermost part of the Tarim Basin lithospheric domain (Figures 6 and 10). The Qilian Shan in the eastern profile and the Tian Shan-Junggar Basin and the Altai Range in the western profile are underlined by Mantle 5, Mantle 3, and Mantle 4, respectively (Figures 6 and 10). This correspondence between tectonic domains at crustal levels and mantle diversity at depth strongly indicates the different origin for these lithospheric terrains constituted by slightly different mantle compositions that collided progressively from north to south to form the wide India-Eurasia Collision Zone.

Interestingly, our results on the compositional variations show that the thickness of Mantle 1 domain is very similar in both selected profiles, but it is grading into hot asthenospheric mantle in the eastern profile (beneath NE Tibet, where the lithospheric mantle is only 90 km thick) and into Mantle 2 PUM (i.e., cold

asthenosphere) in the western profile (beneath Tarim Basin, where the lithospheric mantle is up to 180 km thick). These variations at depth could be related to different stages of the northward advance of the Indian plate beneath Eurasia. To the east, the still active Indian subduction could keep alive corner flow processes maintaining a hot asthenospheric wedge beneath the Tibetan Plateau, which thinned out the lithospheric mantle. To the west, the absence of presently active subduction of India together with the different thicknesses and compositions of Indian and Tarim Basin lithospheric mantle domains indicates a different geodynamic scenario. The Mantle 2 PUM body beneath the Tarim Basin in the western profile, however, might be related to either an inherited influence of precollision processes or linked to the India-Eurasia collision. In the first hypothesis, the fertile composition of Mantle 2 PUM might be inherited from older processes that occurred before the India-Eurasia collision (e.g., Late Carboniferous-Permian large igneous activity) [Chen *et al.*, 2014]. In the second hypothesis, the composition of Mantle 2 PUM could be related to the cessation of a former corner flow activity through a slab break-off and consequent partial thermal recovery of the asthenospheric wedge. This slab break-off is estimated to have occurred at the onset of the India indentation (~45 Ma) [Negredo *et al.*, 2007], and the detached slab should be currently located at depths of ~1100 km below the Tibetan Plateau, as shown in published tomography images [Replumaz *et al.*, 2010, 2014]. Following this second interpretation, we can speculate that the lithospheric structures of the eastern and western profiles represent, respectively, the pre-break-off phase and the post break-off phase of the India subduction beneath Eurasia.

The Indian continental mantle extends ~600 km farther north of the Main Frontal Thrust deepening progressively from ~225 km beneath the foreland to ~300 km close to Karakax Fault and shows a slight thickening (30–50 km) in both transects. The length of the Indian lithosphere beneath the Himalaya and Tibetan Plateau is of same order of magnitude than calculated shortening in the crustal domains [e.g., DeCelles *et al.*, 2002; Replumaz and Tapponnier, 2003; van Hinsbergen *et al.*, 2011, 2012]. In fact, ~600 km of Indian lithospheric mantle is a minimum calculation of its total length if we consider that the original geometry of the mantle should have been thinner toward the edge of its continental passive margin. If true, this slight increase in thickness toward the north could be related to tectonic thickening during collision.

A final piece of information is provided by the combination of our lithospheric models and the seismic tomography (Figure 10). As indicated, the western profile shows an abrupt northern termination of the Indian lithospheric mantle in both, our model and tomography models. In contrast, the eastern profile shows a low angle and north dipping positive anomaly that can be interpreted as the Indian oceanic slab still attached to the Indian continental lithosphere. This slab tomographic image is not observed in the western profile where the Indian oceanic lithosphere has been detached after a break-off event as has been discussed.

## 7. Conclusions

An integrated geophysical-petrological modeling was performed along a 2-D profile crossing the western Himalayan orogen and Tibetan Plateau, the Tarim Basin, the Junggar and Tian Shan, and ending at the southern Altai Range. We compared the results with an updated 2-D lithospheric model crossing the eastern Himalayan orogen and Tibetan Plateau, to consistently discuss the differences along the strike of the India-Eurasia collisional system. The presented cross sections are the first lithospheric models in the India-Eurasia collision zone which combine gravity, geoid, elevation, thermal analysis, mantle petrology, and mantle seismic velocities.

Along the western transect (Profile A-B) the Indian Moho is progressively deepening from ~40 km depth beneath the foreland to ~90 km depth below the Kunlun Shan. Crustal roots are modeled in the Tian Shan and Altai ranges, with the crust-mantle boundary located at ~66 km and ~62 km depth, respectively. The lithosphere shows a gradual thickening from 230 km below the Himalayan foreland to 260 km below the Himalayan orogen and 295 km below the Kunlun Shan. Between the Tibetan Plateau and the Tarim Basin the LAB shows a step-like geometry shallowing ~65 km beneath the Tarim Basin and reaching 230 km depth. The LAB depth increases to ~260 km beneath the Tian Shan and Junggar Basin and to ~270 km below the Altai Range. Along-profile compositional variations within the lithospheric mantle are required to fit the observables. The resulting mantle composition and thickness suggest the presence of four lithospheric mantle domains along this transect. (i) The Indian lithospheric mantle, which underlies the Himalayan foreland basin, the Himalayan orogen, the Tibetan Plateau, and the Kunlun Shan, and it is compatible with a generic

Iherzolitic mantle. The India and Eurasia plates are separated by a sharp change in both LAB and Moho depths, coinciding with the Karakax fault. (ii) The Tarim (Eurasian) lithospheric mantle plunging northward below the Tian Shan. It is underlined by a sublithospheric thermal anomaly (below 300 km depth), likely linked to the enrichment in incompatible elements (CaO and  $\text{Al}_2\text{O}_3$ ) of the deepest lithosphere mantle portion of the Tarim domain. (iii) The Junggar domain characterized by a less dense and seismically slow lithospheric mantle. (iv) A northern lithospheric mantle domain beneath the Altai Range.

Along the eastern transect (Profile C-D) our results confirm that the Eastern Tibetan Plateau is supported by a thick lithosphere (~280 km) in the south and a thin lithosphere (~140 km) in the north. In our interpretation, the Indian lithospheric mantle is underthrusting the Tibetan Plateau up to the Bangong-Nujiang Suture discontinuity, whereas the lithospheric mantle below the Qaidam Basin, Qilian Shan, and North China Block belongs to the Eurasian plate. In between, a transitional lithospheric mantle region, characterized by different thickness, underlies the Qiangtang and partially the north Lhasa terrain. The lithospheric mantle beneath the Qaidam Basin and Qilian Shan is denser and characterized by higher content in FeO, CaO, and also moderately in  $\text{Al}_2\text{O}_3$ .

Both profiles show laterally varying lithospheric mantle structures in terms of lithospheric thickness, lithospheric mantle density, temperature, and composition. The lithospheric mantle in the western transect (Profile A-B) is, in average, colder and thicker than in the eastern one (Profile C-D). The resulting compositional changes in the lithospheric mantle indicate that the Indian plate is chemically more homogeneous than the Eurasian plate. A generic Iherzolitic mantle is compatible with the lithospheric mantle beneath the Himalayan-Tibetan Plateau, whereas relative enrichments of Fe, Ca, and Al oxides are required beneath the Eurasian domains northward, which are compatible with metasomatic processes due to melt circulation.

#### Acknowledgments

The present work has been supported by ATIZA (CGL2009-09662-BTE), TECLA (CGL2011-26670), and MITE (CGL2014-59516-P) projects. This is contribution 618 from the ARC Centre of Excellence for Core to Crust Fluid Systems and 1005 in the GEMOC Key Centre (ARC grant DP120102372). We thank the Editor, Anne Replumaz, and the anonymous Reviewers which largely help to improve the initial manuscript. The data used in this work are available online from <ftp://topex.ucsd.edu/pub/>, <http://www.heatflow.und.edu/>, <http://www.ngdc.noaa.gov/mgg/global/global.html>, and <http://www.earthchem.org/petdb>. Figures were created with GMT [Wessel and Smith, 1995] and/or with Canvas drawing program (Figures 5 and 10).

#### References

- Afonso, J. C., and S. Zlotnik (2011), The subductability of the continental lithosphere: The before and after story, in *Arc-Continent Collision*, *Frontiers in Earth Sciences*, edited by D. Brown, and P. D. Ryan, pp. 53–86, Springer, Berlin, doi:10.1007/978-3-540-88558.
- Afonso, J. C., G. Ranalli, and M. Fernandez (2005), Thermal expansivity and elastic properties of the lithospheric mantle: Results from mineral physics of composites, *Phys. Earth Int.*, 149, 279–306.
- Afonso, J. C., M. Fernández, G. Ranalli, W. L. Griffin, and J. A. D. Connolly (2008), Integrated geophysical-petrological modeling of the lithosphere and sub-lithospheric upper mantle: Methodology and applications, *Geochem. Geophys. Geosyst.*, 9, Q05008, doi:10.1029/2007GC001834.
- Afonso, J. C., J. Fullea, W. L. Griffin, Y. Yang, A. G. Jones, J. A. D. Connolly, and S. Y. O'Reilly (2013a), 3-D multi-observable probabilistic inversion for the compositional and thermal structure of the lithosphere and upper mantle. I: A priori petrological information and geophysical observables, *J. Geophys. Res. Solid Earth*, 118, 2586–2617, doi:10.1002/jgrb.50124.
- Afonso, J. C., J. Fullea, Y. Yang, J. A. D. Connolly, and A. G. Jones (2013b), 3-D multi-observable probabilistic inversion for the compositional and thermal structure of the lithosphere and upper mantle. II: General methodology and resolution analysis, *J. Geophys. Res. Solid Earth*, 118, 1650–1676, doi:10.1002/jgrb.50123.
- Amante, C., and B. W. Eakins (2009), ETOPO1 arc-minute global relief model: Procedures, data sources and analysis, *NOAA Tech. Memo. NESDIS NGDC-24*, 19 pp. [Available at <http://www.ngdc.noaa.gov>.]
- An, M., and Y. Shi (2006), Lithospheric thickness of the Chinese continent, *Phys. Earth Planet. Inter.*, 159, 257–266.
- An, M., and Y. Shi (2007), Three-dimensional thermal structure of the Chinese continental crust and upper mantle, *Sci. China Earth Sci.*, 50(10), 1441–1451.
- Artemieva, I. (2011), *The Lithosphere: An Interdisciplinary Approach*, 773 pp., Cambridge Univ. Press, Cambridge.
- Artemieva, I. M. (2006), Global 1 × 1 thermal model TC1 for the continental lithosphere: Implications for lithosphere secular evolution, *Tectonophysics*, 426, 245–277.
- Bagdassarov, N., V. Batalev, and V. Egorova (2011), State of lithosphere beneath Tien Shan from petrology and electrical conductivity of xenoliths, *J. Geophys. Res.*, 116, B01202, doi:10.1029/2009JB007125.
- Bai, Z., S. Zhang, and C. Braitenberg (2013), Crustal density structure from 3D gravity modeling beneath Himalaya and Lhasa blocks, Tibet, *J. Asian Earth Sci.*, 78, 301–317, doi:10.1016/j.jseas.2012.12.035.
- Basuyau, C., M. Diamant, C. Tiberi, G. Hetényi, J. Vergne, and A. Peyrefitte (2013), Joint inversion of teleseismic and GOCE gravity data: Application to the Himalayas, *Geophys. J. Int.*, 193(1), 149–160.
- Bell, D. R., M. Gregoire, T. L. Grove, N. Chatterjee, R. W. Carlson, and P. R. Buseck (2005), Silica and volatile-element metasomatism of Archean mantle: A xenolith-scale example from the Kaapvaal Craton, *Contrib. Mineral. Petrol.*, 150(3), 251–267.
- Belousov, V. V., N. I. Pavlenkova, and G. N. Kvyatkovskaya (1992), Structure of the crust and upper mantle of the (former) USSR, *Int. Geol. Rev.*, 34(3), 213–216, doi:10.1080/00206819209465597.
- Bijwaard, H., W. Spakman, and E. R. Engdahl (1998), Closing the gap between regional and global travel time tomography, *J. Geophys. Res.*, 103, 30,055–30,078, doi:10.1029/98JB02467.
- Bowin, C. (2000), Mass anomalies and the structure of the Earth, *Phys. Chem. Earth*, 25(4), 343–353.
- Braitenberg, C., M. Zadro, J. Fang, Y. Wang, and H. T. Hsu (2000), The gravity and isostatic Moho undulations in Qinghai-Tibet plateau, *J. Geodyn.*, 30(5), 489–505.
- Braitenberg, C., Y. Wang, J. Fang, and H. T. Hsu (2003), Spatial variations of flexure parameters over the Tibet-Qinghai Plateau, *Earth Planet. Sci. Lett.*, 205, 211–224.
- Cao, R. L., and S. H. Zhu (1987), Mantle xenoliths and alkali-rich host rocks in eastern China, in *Mantle Xenoliths*, edited by P. H. Nixon, pp. 167–180, Wiley, New York.



- Carballo, A., M. Fernandez, M. Torne, I. Jimenez-Munt, and A. Villaseñor (2015a), Thermal and petrophysical characterization of the lithospheric mantle along the northeastern Iberia geo-Transect, *Gondwana Res.*, **27**, 1430–1445, doi:10.1016/j.gr.2013.12.012.
- Carballo, A., et al. (2015b), From the North-Iberian Margin to the Alboran Basin: A lithosphere geo-transect across the Iberian Plate, *Tectonophysics*, **663**, 399–418, doi:10.1016/j.tecto.2015.07.009.
- Ceylan, S., J. Ni, J. Y. Chen, Q. Zhang, F. Tilmann, and E. Sandvol (2012), Fragmented Indian plate and vertically coherent deformation beneath eastern Tibet, *J. Geophys. Res.*, **117**, B11303, doi:10.1029/2012JB009210.
- Chan, G. H. N., D. J. Waters, M. P. Searle, J. C. Aitchison, M. S. A. Horstwood, Q. Crowley, C. H. Lo, and J. S. L. Chan (2009), Probing the basement of southern Tibet: Evidence from crustal xenoliths entrained in a Miocene ultrapotassic dyke, *Geol. Soc. London J.*, **166**, 45–52, doi:10.1144/0016-76492007-145.
- Charvet, J., L. S. Shu, S. Laurent-Charvet, B. Wang, F. Michel, C. Dominique, Y. Chen, and D. J. Koen (2011), Paleozoic tectonic evolution of the Tianshan belt, NW China, *Sci. China Earth Sci.*, **54**(2), 166–184.
- Chen, B., J. Liu, C. Chen, J. Du, and Y. Sun (2015), Elastic thickness of the Himalayan–Tibetan orogen estimated from the fan wavelet coherence method, and its implications for lithospheric structure, *Earth Planet. Sci. Lett.*, **409**, 1–14, doi:10.1016/j.epsl.2014.10.039.
- Chen, M.-M., W. Tian, K. Suzuki, M.-L.-G. Tejada, F. L. Liu, R. Senda, C.-J. Wei, B. Chen, and Z. Y. Chu (2014), Peridotite and pyroxenite xenoliths from Tarim, NW China: Evidences for melt depletion and mantle refertilization in the mantle source region of the Tarim flood basalt, *Lithos*, doi:10.1016/j.lithos.2014.01.005.
- Chen, Y., F. Niu, R. Liu, Z. Huang, H. Tkalcic, L. Sun, and W. Chan (2010), Crustal structure beneath China from receiver function analysis, *J. Geophys. Res.*, **115**, 2156–2202, doi:10.1029/2009JB006386.
- Chen, Y., W. Li, X. Yuan, J. Badal, and J. Teng (2015), Tearing of the Indian lithospheric slab beneath southern Tibet revealed by SKS-wave splitting measurements, *Earth Planet. Sci. Lett.*, **413**, 13–24, doi:10.1016/j.epsl.2014.12.041.
- Connolly, J. (2005), Computation of phase equilibria by linear programming: A tool for geodynamic modeling and an application to subduction zone decarbonation, *Earth Planet. Sci. Lett.*, **236**, 524–541.
- DeCelles, P. G., D. M. Robinson, and G. Zandt (2002), Implications of shortening in the Himalayan fold-thrust belt for uplift of the Tibetan Plateau, *Tectonics*, **21**(6), 1062, doi:10.1029/2001TC001322.
- Dewey, J. F., R. M. Shackleton, C. Chengfa, and S. Yiyin (1988), The tectonic evolution of the Tibetan plateau, *Philos. Trans. R. Soc. London*, **327**, 379–413.
- Ding, L., P. Kapp, Y. Yue, and Q. Lai (2007), Postcollisional calc-alkaline lavas and xenoliths from the southern Qiangtang terrane, central Tibet, *Earth Planet. Sci. Lett.*, **254**, 28–38.
- Eaton, D. W., F. Darbyshire, R. L. Evans, H. Grütter, A. G. Jones, and X. Yuan (2009), The elusive lithosphere–asthenosphere boundary (LAB) beneath cratons, *Lithos*, **109**, 1–22.
- El Messbahi, H., J.-L. Bodinier, A. Vauchez, J. M. Dautria, H. Ouali, and C. J. Garrido (2015), Short wavelength lateral variability of lithospheric mantle beneath the Middle Atlas (Morocco) as recorded by mantle xenoliths, *Tectonophysics*, **650**, 34–52.
- Engdahl, E. R., R. van der Hilst, and R. P. Buland (1998), Global teleseismic earthquake relocation with improved travel times and procedures for depth determination, *Bull. Seismol. Soc. Am.*, **88**, 3295–3314.
- England, P. C., and P. Molnar (1997), Active deformation of Asia: From kinematics to dynamics, *Science*, **278**, 647–650.
- Feng, M., and M. An (2010), Lithospheric structure of the Chinese mainland determined from joint inversion of regional and teleseismic Rayleigh-wave group velocities, *J. Geophys. Res.*, **115**, B06317, doi:10.1029/2008JB005787.
- Fullea, J., M. Fernández, and H. Zeyen (2008), FA2BOUG - A FORTRAN 90 code to compute Bouguer gravity anomalies from gridded free-air anomalies: Application to the Atlantic-Mediterranean transition zone, *Comput. Geosci.*, **34**(12), 1665–1681, doi:10.1016/j.cageo.2008.02.018.
- Fullea, J., J. C. Afonso, J. A. D. Connolly, M. Fernández, D. García-Castellanos, and H. Zeyen (2009), LitMod 3D: An interactive 3D software to model the thermal, compositional, density, seismological, and rheological structure of the lithosphere and sublithospheric upper mantle, *Geochem. Geophys. Geosyst.*, **10**, Q08019, doi:10.1029/2009GC002391.
- Galvé, A., M. Jiang, A. Hirn, M. Sapin, M. Laigle, B. de Voogd, J. Gallart, and H. Qian (2006), Explosion seismic *P* and *S* velocity and attenuation constraints on the lower crust of the North-Central Tibetan Plateau, and comparison with the Tethyan Himalayas: Implications on composition, mineralogy, temperature, and tectonic evolution, *Tectonophysics*, **412**, 141–157.
- Gao, C., and D. Ye (1997), Petroleum geology of the Tarim Basin, NW China: Recent advances, *J. Pet. Geol.*, **20**(2), 239–244.
- Gaul, O. F., W. L. Griffin, S. Y. O'Reilly, and N. J. Pearson (2000), Mapping olivine composition in the lithospheric mantle, *Earth Planet. Sci. Lett.*, **182**, 223–235.
- Griffin, W. L., S. Y. O'Reilly, C. G. Ryan, O. Gaul, and D. Ionov (1998), Secular variation in the composition of subcontinental lithospheric mantle, in *Structure and Evolution of the Australian Continent*, *Geodyn. Ser.*, vol. 26, edited by J. Braun et al., pp. 1–26, AGU, Washington, D. C.
- Griffin, W. L., S. Y. O'Reilly, and C. G. Ryan (1999), The composition and origin of subcontinental lithospheric mantle, in *Mantle Petrology: Field Observations and High Pressure Experimentation: A Tribute to Francis F. (Joe) Boyd*, edited by Y. Fei, C. M. Bertka, and B. O. Mysen, pp. 13–45, The Geochem. Soc., Washington, D. C.
- Griffin, W. L., N. J. Pearson, E. Belousova, S. E. Jackson, E. Van Acherterbergh, S. Y. O'Reilly, and S. R. Shee (2000), The Hf isotope composition of cratonic mantle: LAM-MC-ICPMS analysis of zircon megacrysts in kimberlites, *Geochim. Cosmochim. Acta*, **64**(1), 133–147.
- Griffin, W. L., S. Y. O'Reilly, N. Abe, S. Aulbach, R. M. Davies, N. J. Pearson, B. J. Doyle, and K. Kivi (2003), The origin and evolution of Archean lithospheric mantle, *Precambrian Res.*, **127**, 19–41.
- Griffin, W. L., S. Y. O'Reilly, J. C. Afonso, and G. C. Begg (2009), The composition and evolution of lithospheric mantle: A re-evaluation and its tectonic implications, *J. Petrol.*, **50**, 1185–1204.
- Groppo, C., B. Lombardo, F. Rolfo, and P. Pertusati (2007), Clockwise exhumation path of granulitized eclogites from the Ama Drime range (eastern Himalayas), *J. Metamorph. Geol.*, **25**, 51–75, doi:10.1111/j.1525-1314.2006.00678.x.
- Grose, C., and J. C. Afonso (2013), Comprehensive plate models for the thermal evolution of oceanic lithosphere, *Geochem. Geophys. Geosyst.*, **14**, 3751–3778, doi:10.1002/ggge.20232.
- Grujic, D., C. J. Warren, and J. Wooden (2011), Rapid syn-convergent exhumation of Miocene-aged lower orogenic crust in the Eastern Himalaya, *Lithosphere*, **3**(5), 346–366, doi:10.1130/L154.1.
- Guillot, S., and A. Replumaz (2013), Importance of continental subductions for the growth of the Tibetan plateau, *Bull. Soc. Géol. Fr.*, **184**(3), 199–223.
- Guillot, S., E. Garzanti, D. Baratoux, D. Marquer, G. Maheo, and J. de Sigoyer (2003), Reconstructing the total shortening history of the NW Himalaya, *Geochem. Geophys. Geosyst.*, **4**(7), 1064, doi:10.1029/2002GC000484.
- Hacker, B. R., E. Gnos, L. Ratschbacher, M. Grove, M. McWilliams, S. V. Sobolev, J. Wan, and W. Zhenhan (2000), Hot and dry deep crustal xenoliths from Tibet, *Science*, **287**, 2463–2466.

- Harris, N. B. W., R. Xu, C. L. Lewis, C. J. Hawkeworth, and Y. Zhang (1988), Isotope geochemistry of the 1985 Tibet Geotraverse, Lhasa to Golmud, *Philos. Trans. R. Soc. London A*, **327**, 263–285.
- Hawkesworth, C. J., D. G. Pearson, and S. P. Turner (1999), Chemical and temporal variations in the Earth's lithosphere, *Philos. Trans. R. Soc. London A*, **357**, 647–669.
- He, R., G. Liu, E. Golos, R. Gao, and H. Zheng (2014), Isostatic gravity anomaly, lithospheric scale density structure of the northern Tibetan plateau and geodynamic causes for potassic lava eruption in Neogene, *Tectonophysics*, **628**, 218–227.
- Hetényi, G., R. Cattin, F. Brunet, L. Bollinger, J. Vergne, J. L. Nabelek, and M. Diament (2007), Density distribution of the India plate beneath the Tibetan Plateau: Geophysical and petrological constraints on the kinetics of lower crustal eclogitization, *Earth Planet. Sci. Lett.*, **264**, 226–244.
- Holland, T., and R. Powell (1998), An internally consistent thermodynamic data set for phases of petrological interest, *J. Metamorph. Geol.*, **16**, 309–343.
- Huang, J., and D. Zhao (2006), High-resolution mantle tomography of China and surrounding regions, *J. Geophys. Res.*, **111**, B09305, doi:10.1029/2005JB004066.
- Husson, K., M. Bernet, S. Guillot, P. Huyghe, J. L. Mugnier, A. Replumaz, X. Robert, P. Van der Beek (2014), Dynamics ups and downs of the Himalaya, *Geology*, **42**, 839–842, doi:10.1130/G36049.1.
- Jackson, J., H. Austrheim, D. McKenzie, and K. Priestley (2004), Metastability, mechanical strength, and the support of mountain belts, *Geology*, **32**, 625–628.
- Jiang, C., J. Yang, B. Feng, Z. Zhu, M. Zhao, Y. C. Chai, X. D. Shi, H. D. Wang, and J. Q. Flu (1992), *Opening-Closing Tectonics of Kunlun Mountains* [in Chinese with English abstract], 224 pp., Geol. House, Beijing.
- Jiang, M., A. Galvé, A. Hirn, B. deVoogd, M. Laigle, H. P. Su, J. Diaz, J. C. Lepine, and Y. X. Wang (2006), Crustal thickening and variations in architecture from the Qaidam Basin to the Qang Tang (North-Central Tibetan Plateau) from wide-angle reflection seismology, *Tectonophysics*, **412**, 121–140.
- Jiménez-Munt, I., and J. P. Platt (2006), Influence of mantle dynamics on the topographic evolution of the Tibetan Plateau: Results from numerical modeling, *Tectonics*, **25**, TC6002, doi:10.1029/2006TC001963.
- Jiménez-Munt, I., M. Fernández, J. Vergés, and J. P. Platt (2008), Lithosphere structure underneath the Tibetan Plateau inferred from elevation, gravity and geoid anomalies, *Earth Planet. Sci. Lett.*, **267**, 276–289, doi:10.1016/j.epsl.2007.11.045.
- Jin, Y., M. K. McNutt, and Y. Zhu (1994), Evidence from gravity and topography data for folding of Tibet, *Nature*, **371**, 669–674.
- Jolivet, M., M. Brunel, D. Seward, Z. Xu, J. Yang, J. Malavieille, F. Roger, A. Leyreloup, N. Arnaud, and C. Wu (2003), Neogene extension and volcanism in the Kunlun Fault Zone, northern Tibet: New constraints on the age of the Kunlun Fault, *Tectonics*, **22**(5), 1052, doi:10.1029/2002TC001428.
- Kao, H., R. Gao, R.-J. Rau, D. Shi, R.-Y. Chen, T. Guan, and F. T. Wu (2001), Seismic image of the Tarim basin and its collision with Tibet, *Geology*, **29**, 575–578.
- Karato, S. I. (1993), Importance of anelasticity in the interpretation of seismic tomography, *Geophys. Res. Lett.*, **20**, 1623–1626, doi:10.1029/93GL01767.
- Kennett, B. L. N., E. R. Engdahl, and R. Buland (1995), Constraints on seismic velocities in the Earth from travel times, *Geophys. J. Int.*, **122**, 108–124.
- Kosarev, G. L., N. V. Petersen, L. P. Vinnik, and S. W. Roecker (1993), Receiver functions for the Tien Shan analog broadband network: Contrasts in the evolution of structures across the Talasso-Fergana fault, *J. Geophys. Res.*, **98**, 4437–4448, doi:10.1029/92JB02651.
- Kumar, P., X. Yuan, R. Kind, and G. Kosarev (2005), The lithosphere-aesthenosphere boundary in the Tien Shan-Karakorum region from S receiver function: Evidence for continental subduction, *Geophys. Res. Lett.*, **32**, L07305, doi:10.1029/2004GL022291.
- Kumar, P., X. Yuan, R. Kind, and J. Ni (2006), Imaging the colliding India and Asian lithospheric plates beneath Tibet, *J. Geophys. Res.*, **111**, B06308, doi:10.1029/2005JB003930.
- Le Pichon, X., P. Henry, and B. Goffée (1999), Uplift of Tibet from eclogites to granulites—Implications for the Andean Plateau and the Variscan belt, *Tectonophysics*, **273**, 57–76.
- Le Roux, V., J.-L. Bodinier, A. Tommasi, O. Alard, J.-M. Dautria, A. Vauchez, and A. J. V. Riches (2007), The Lherz spinel lherzolite: Refertilised rather than pristine mantle, *Earth Planet. Sci. Lett.*, **259**, 599–612.
- Lei, J. (2011), Seismic tomographic imaging of the crust and upper mantle under the central and western Tien Shan orogenic belt, *J. Geophys. Res.*, **116**, B09305, doi:10.1029/2010JB008000.
- Lei, J., and D. Zhao (2007), Teleseismic P-wave tomography and the upper mantle structure of the central Tien Shan orogenic belt, *Phys. Earth Planet. Inter.*, **162**, 165–185.
- Lenardic, A., and L.-N. Moresi (1999), Some thoughts on the stability of cratonic lithosphere: Effects of buoyancy and viscosity, *J. Geophys. Res.*, **104**, 12,747–12,758, doi:10.1029/1999JB900035.
- Li, C., R. van der Hilst, A. Meltzer, and E. Engdahl (2008), Subduction of the Indian lithosphere beneath the Tibet Plateau and Burma, *Earth Planet. Sci. Lett.*, **274**, 157–168.
- Li, S., W. D. Mooney, and J. Fan (2006), Crustal structure of mainland China from deep seismic sounding data, *Tectonophysics*, **420**, 239–252.
- Li, Y., Q. Liu, J. Chen, S. Li, B. Guo, and Y. Lai (2007), Shear wave velocity structure of the crust and upper mantle underneath the Tianshan orogenic belt, *Sci. China Earth Sci.*, **50**(3), 321–330.
- Liang, X., Y. Shen, Y. J. Chen, and Y. Ren (2011), Crustal and mantle velocity models of southern Tibet from finite frequency tomography, *J. Geophys. Res.*, **116**, B02408, doi:10.1029/2009JB007159.
- Liang, X., E. Sandvol, Y. J. Chen, T. Hearn, J. Ni, S. Klemperer, Y. Shen, and F. Tilmann (2012), A complex Tibetan upper mantle: A fragmented Indian slab and no south-verging subduction of Eurasian lithosphere, *Earth Planet. Sci. Lett.*, **333–334**, 101–111, doi:10.1016/j.epsl.2012.03.036.
- Liu, S., L. Wang, C. Li, H. Li, Y. Han, C. Jia, and G. Wei (2004), Thermal-rheological structure of lithosphere beneath the northern flank of Tarim Basin, western China: Implication for geodynamics, *Sci. China, Ser. D: Earth Sci.*, **47**(7), 659–672.
- Liu, Z. Q. (1988), *Geological Map of the Qinghai-Xizang Plateau and Its Neighboring Regions (Scale at: 1,500,000)*, Chengdu Inst. of Geol. and Miner. Resour., Geol. House, Beijing.
- Lu, S. N., H. K. Li, C. L. Zhang, and G. H. Niu (2008), Geological and geochronological evidence for the Precambrian evolution of the Tarim craton and surrounding continental fragments, *Precambrian Res.*, **160**, 94–107.
- Masce, G., A. Pecher, S. Guillot, S. M. Rai, and A. P. Gajurel (2012), *The Himalaya-Tibet Collision*, 264 pp., Ed. Nepal Geol. Soc., Soc. Geol. de Fr., Vuibert.
- McDonough, W. F., and S.-s. Sun (1995), The composition of the Earth, *Chem. Geol.*, **120**, 223–253.
- McNamara, D. E., W. R. Walter, T. J. Owens, and C. J. Ammon (1997), Upper mantle velocity structure beneath the Tibetan Plateau from Pn travel time tomography, *J. Geophys. Res.*, **102**, 493–505, doi:10.1029/96JB02112.

- Mechie, J., S. V. Sobolev, L. Ratschbacher, A. Y. Babeiko, G. Bock, A. G. Jones, K. D. Nelson, K. D. Solon, L. D. Brown, and W. Zhao (2004), Precise temperature estimation in the Tibetan crust from seismic detection of the  $\alpha$ - $\beta$  quartz transition, *Geology*, **32**, 601–604.
- Mechie, J., et al. (2012), Crustal and uppermost mantle velocity structure along a profile across the Pamir and southern Tien Shan as derived from project TIPAGE wide-angle seismic data, *Geophys. J. Int.*, **188**, 385–407, doi:10.1111/j.1365-246X.2011.05278.x.
- Mitra, S., K. Priestley, A. K. Bhattacharya, and V. K. Gaur (2005), Crustal structure and earthquake focal depths beneath northeastern India and southern Tibet, *Geophys. J. Int.*, **160**, 227–248.
- Mohanty, D., A. Singh, L. O'Driscoll, M. Ravi Kumar, D. Srinagesh, and E. D. Humphreys (2016), P-wave velocity structure below India and Tibet incorporating anisotropic delay time effects, *Geochem. Geophys. Geosyst.*, **17**, 725–738, doi:10.1002/2015GC006064.
- Molnar, P., and P. Tapponnier (1975), Cenozoic tectonics of Asia: Effects of a continental collision, *Science*, **189**(4201), 419–426, doi:10.1126/science.189.4201.419.
- Nabelek, J., G. Hetenyi, J. Vergne, S. Sapkota, B. Kafle, M. Jiang, H. Su, J. Chen, B. S. Huang, and Hi-CLIMB Team (2009), Underplating in the Himalaya-Tibet collision zone revealed by the Hi-CLIMB experiment, *Science*, **325**, 1371–1374, doi:10.1126/science.1167719.
- Negredo, A. M., A. Replumaz, A. Villaseñor, and S. Guillot (2007), Modeling the evolution of continental subduction processes in the Pamir-Hindu Kush region, *Earth Planet. Sci. Lett.*, **259**, 212–225, doi:10.1016/j.epsl.2007.04.043.
- Nelson, K. D., et al. (1996), Partially molten middle crust beneath southern Tibet: Synthesis of project INDEPTH results, *Science*, **274**(5293), 1684–1688, doi:10.1126/science.274.5293.1684.
- O'Reilly, S. Y., and W. L. Griffin (2006), Imaging chemical and thermal heterogeneity in the sub-continental lithospheric mantle with garnets and xenoliths. Geophysical implications, *Tectonophysics*, **416**, 289–309.
- O'Reilly, S. Y., W. L. Griffin, Y. H. Poudjom-Djomani, and P. Morgan (2001), Are lithospheres forever? Tracking changes in subcontinental lithospheric mantle through time, *GSA Today*, **11**, 4–10.
- Owens, T. J., and G. Zandt (1997), Implications of crustal property variations for models of Tibetan plateau evolution, *Nature*, **387**, 37–42.
- Pavlis, N. K., S. A. Holmes, S. C. Kenyon, and J. K. Factor (2008), An Earth gravitational model to degree 2160: EGM2008, *Geophys. Res. Abstr.*, **10**, EGU2008-A-01891.
- Pearson, D. G., S. B. Shirey, R. W. Carlson, F. R. Boyd, N. P. Pokhilenko, and N. Shimizu (1995), Re-Os, Sm-Nd, and Rb-Sr isotope evidence for thick Archaean lithospheric mantle beneath the Siberian craton modified by multistage metasomatism, *Geochim. Cosmochim. Acta*, **59**(5), 959–977.
- Pedreira, D., J. C. Afonso, J. A. Pulgar, J. Gallastegui, A. Carballo, M. Fernández, D. García-Castellanos, I. Jiménez-Munt, J. Semprich, and O. García-Moreno (2015), Geophysical-petrological modelling of the lithosphere beneath Cantabrian Mountains and the North-Iberian margin: Geodynamic implications, *Lithos*, **46**–48.
- Pollack, H. N., S. J. Hurter, and J. R. Johnson (1993), Heat-flow from the Earth's interior-analysis of the global data set, *Rev. Geophys.*, **31**, 267–280, doi:10.1029/93RG01249.
- Poudjom-Djomani, Y. H., S. Y. O'Reilly, W. L. Griffin, and P. Morgan (2001), The density structure of subcontinental lithosphere through time, *Earth Planet. Sci. Lett.*, **184**, 605–621.
- Poupinet, G., et al. (2002), Intracontinental subduction and Palaeozoic inheritance of the lithosphere suggested by a teleseismic experiment across the Chinese Tien Shan, *Terra Nova*, **14**(1), 18–24.
- Priestley, K., and D. McKenzie (2006), The thermal structure of the lithosphere from shear wave velocities, *Earth Planet. Sci. Lett.*, **244**, 285–301.
- Priestley, K., J. Jackson, and D. McKenzie (2008), Lithospheric structure and deep earthquakes beneath India, the Himalaya and southern Tibet, *Geophys. J. Int.*, **172**, 345–362, doi:10.1111/j.1365-246X.2007.03636.x.
- Pubellier, M., N. Chamot-Rooke, F. Ego, J. C. Guezou, E. Konstantinovskaya, A. Rabaute, and J. C. Ringenbach (2008), Structural map of Eastern Eurasia, Comm. for the Geol. Map of the World (CGMW), Paris.
- Rai, S., K. Priestley, V. Gaur, S. Mitra, M. Singh, and M. P. Searle (2006), Configuration of the Indian Moho beneath the Northwest Himalaya and Ladakh, *Geophys. Res. Lett.*, **33**, L15308, doi:10.1029/2006GL026076.
- Ren, Y., and Y. Shen (2008), Finite frequency tomography in southeastern Tibet: Evidence for the causal relationship between mantle lithosphere delamination and the north-south trending rifts, *J. Geophys. Res.*, **113**, B10316, doi:10.1029/2008JB005615.
- Replumaz, A., and P. Tapponnier (2003), Reconstruction of the deformed collision zone between India and Asia by backward motion of lithospheric blocks, *J. Geophys. Res.*, **108**(B6), 2285, doi:10.1029/2001JB000661.
- Replumaz, A., A. M. Negredo, S. Guillot, and A. Villaseñor (2010), Multiple episodes of continental subduction during India/Asia convergence: Insight from seismic tomography and tectonic reconstruction, *Tectonophysics*, doi:10.1016/j.tecto.2009.10.007.
- Replumaz, A., S. Guillot, A. Villaseñor, and A. M. Negredo (2013), Amount of Asian lithospheric mantle subducted during the India/Asia collision, *Gondwana Res.*, **24**, 936–945.
- Replumaz, A., F. Capitanio, S. Guillot, A. Negredo, and A. Villaseñor (2014), The coupling of Indian subduction and Asian continental tectonics, *Gondwana Res.*, doi:10.1016/j.gr.2014.04.003.
- Robert, A. M. M., M. Fernández, I. Jiménez-Munt, and J. Vergés (2016), Lithospheric structure in Central Eurasia derived from elevation, geoid anomaly and thermal analysis, *Geol. Soc. London, Spec. Publ.*, **427**, doi:10.1144/SP427.10.
- Sandwell, D. T., and H. W. F. Smith (1997), Marine gravity anomalies from GEOSAT and ERS-1 satellite altimetry, *J. Geophys. Res.*, **102**, 10,039–10,054, doi:10.1029/96JB03223.
- Schubert, G., D. L. Turcotte, and P. Olson (2001), *Mantle Convection in the Earth and Planets*, 940 pp., Cambridge Univ. Press, Cambridge, U. K.
- Schulte-Pelkum, V., G. Monsalve, A. Sheehan, M. R. Pandey, S. Sapkota, R. Bilham, and F. Wu (2005), Imaging the Indian subcontinent beneath the Himalaya, *Nature*, **435**, 1222–1225.
- Searle, M. P. (2010), Geological evolution of the Karakoram ranges, *Ital. J. Geosci. (Boll. Soc. Geol. Ital.)*, **130**(2), 147–159, doi:10.3301/IUG.2011.08.
- Shi, D., W. Zhenhan, S. L. Klemperer, W. Zhao, G. Xue, and H. Sue (2015), Receiver function imaging of crustal suture, steep subduction, and mantle wedge in the eastern India-Tibet continental collision zone, *Earth Planet. Sci. Lett.*, **414**, 6–15.
- Shin, Y. H., H. Xu, C. Braitenberg, J. Fang, and Y. Wang (2007), Moho undulations beneath Tibet from GRACE-integrated gravity data, *Geophys. J. Int.*, **170**, 971–985, doi:10.1111/j.1365-246X.2007.03457.x.
- Song, S. G., L. Su, Y. L. Niu, and L. F. Zhang (2007), Petrological and geochemical constraints on the origin of garnet peridotite in the North Qaidam ultrahigh-pressure Metamorphic Belt, Northwestern China, *Lithos*, **96**, 243–265.
- Steffen, R., H. Steffen, and G. Jentzsch (2011), A three-dimensional Moho depth model for the Tien Shan from EGM2008 gravity data, *Tectonics*, **30**, TC5019, doi:10.1029/2011TC002886.
- Tapponnier, P., X. Zhiqin, F. Roger, B. Meyer, N. Arnaud, G. Wittlinger, and Y. Jingsui (2001), Oblique stepwise rise and growth of the Tibet Plateau, *Science*, **294**(5547), 1671–1677, doi:10.1126/science.105978.

- Tenze, D., C. Braitenberg, and E. Sinchic (2014), Detecting the elevated crust to mantle section in the Kohistan-Ladakh Arc, Himalaya, from GOCE observations, in *Gravity, Geoid and Height Systems, Proceedings of the IAG Symposium Gghs2012, October 9-12, 2012, Venice, Italy*, edited by U. Marti, pp. 299–307, Springer, New York.
- Tilmann, F., J. Ni, and INDEPTH III Seismic Team (2003), Seismic imaging of the downwelling Indian lithosphere beneath central Tibet, *Science*, **300**, 1424–1427, doi:10.1126/science.1082777.
- Tunini, L., I. Jiménez-Munt, M. Fernandez, J. Vergés, and A. Villaseñor (2015), Lithospheric mantle heterogeneities below the Zagros Mountains and the Iranian Plateau: A petrological-geophysical study, *Geophys. J. Int.*, **200**, 596–614.
- Van der Voo, R., W. Spakman, and H. Bijwaard (1999), Tethyan subducted slabs under India, *Earth Planet. Sci. Lett.*, **171**, 7–20.
- van Hinsbergen, D. J., P. Kapp, G. Dupont-Nivet, P. C. Lippert, P. G. DeCelles, and T. H. Torsvik (2011), Restoration of Cenozoic deformation in Asia and the size of Greater India, *Tectonics*, **30**, TC5003, doi:10.1029/2011TC002908.
- van Hinsbergen, D. J., P. C. Lippert, G. Dupont-Nivet, N. McQuarrie, P. V. Doubrovine, W. Spakman, and T. H. Torsvik (2012), Greater India Basin hypothesis and a two-stage Cenozoic collision between India and Asia, *Proc. Natl. Acad. Sci. U.S.A.*, **109**, 7659–7664, doi:10.1073/pnas.1117262109.
- Vergne, J., G. Wittlinger, Q. Hui, P. Tapponnier, G. Poupinet, J. Mei, G. Herquel, and A. Paul (2002), Seismic evidence for stepwise thickening of the crust across the NE Tibetan Plateau, *Earth Planet. Sci. Lett.*, **203**, 25–33.
- Vilà, M., M. Fernández, and I. Jiménez-Munt (2010), Radiogenic heat production variability of some common lithological groups and its significance to lithospheric thermal modeling, *Tectonophysics*, **490**, 152–164, doi:10.1016/j.tecto.2010.05.003.
- Villaseñor, A., W. Spakman, and E. R. Engdahl (2003), Influence of regional travel times in global tomographic models, EGS-AGU-EUG Joint Assembly, Nice.
- Vinnik, L. P., C. Reigber, I. M. Aleshin, G. L. Koserev, M. K. Kaban, S. I. Oreshin, and S. W. Roecker (2004), Receiver function tomography of the central Tien Shan, *Earth Planet. Sci. Lett.*, **225**, 131–146, doi:10.1016/j.epsl.2004.05.039.
- Vozar, J., A. G. Jones, J. Fulla, M. R. Agius, S. Lebedev, F. Le Pape, and W. Wei (2014), Integrated geophysical-petrological modeling of lithosphere-asthenosphere boundary in central Tibet using electromagnetic and seismic data, *Geochem. Geophys. Geosyst.*, **15**, 3965–3988, doi:10.1002/2014GC005365.
- Wang, T., D. W. Hong, B. M. Jahn, Y. Tong, Y. B. Wang, B. F. Han, and X. X. Wang (2006), Zircon U-Pb geochronology and geochemistry of Paleozoic synorogenic intrusions from the Chinese Altai: Implications for subduction-accretion processes, *J. Geol.*, **114**, 735–751.
- Wang, Y. (2001), Heat flow pattern and lateral variations of lithosphere strength in China mainland: Constraints on active deformation, *Phys. Earth Planet. Inter.*, **126**, 121–146.
- Wang, Y., W. D. Mooney, X. Yuan, and R. G. Coleman (2003), The crustal structure from the Altai Mountains to the Altyn Tagh fault, northwest China, *J. Geophys. Res.*, **108**(B6), 2322, doi:10.1029/2001JB000552.
- Warren, C. J., D. Grujic, D. Kellett, J. Cottle, R. A. Jamieson, and K. S. Ghalley (2011), Probing the depths of the India-Asia collision: U-Th-Pb monazite chronology of granulites from NW Bhutan, *Tectonics*, **30**, TC2004, doi:10.1029/2010TC002738.
- Wessel, P., and W. H. F. Smith (1995), New version of the Generic Mapping Tools released, *Eos Trans. AGU*, **76**, 329, doi:10.1029/95EO00198.
- Wittlinger, G., V. Farra, and J. Vergne (2004), Lithospheric and upper mantle stratifications beneath Tibet: New insights from Sp conversions, *Geophys. Res. Lett.*, **31**, L19615, doi:10.1029/2004GL020955.
- Wittlinger, G., V. Farra, G. Hetényi, J. Vergne, and J. Nábělek (2009), Seismic velocities in southern Tibet lower crust: A receiver function approach for eclogite detection, *Geophys. J. Int.*, **177**, 1037–1049.
- Xu, Y., F. Liu, J. Liu, and H. Chen (2002), Crust and upper mantle structure beneath western China from P wave travel time tomography, *J. Geophys. Res.*, **107**(B10), 2220, doi:10.1029/2001JB000402.
- Xu, Y.-G., X. Wei, Z.-Y. Luo, H.-Q. Liu, and J. Cao (2014), The Early Permian Tarim Large Igneous Province: Main characteristics and a plume incubation model, *Lithos*, doi:10.1016/j.lithos.2014.02.015.
- Yin, A., and T. M. Harrison (2000), Geologic evolution of the Himalayan-Tibetan orogen, *Annu. Rev. Earth Planet. Sci.*, **28**, 211–280.
- Yuan, H., and B. Romanowicz (2010), Lithospheric layering in the North American craton, *Nature*, **466**, 1063–1068.
- Yue, H., et al. (2012), Lithospheric and upper mantle structure of the northeastern Tibetan Plateau, *J. Geophys. Res.*, **117**, B05307, doi:10.1029/2011JB008545.
- Zeng, S., X. Hu, J. Li, S. Xu, H. Fang, and J. Cai (2015), Detection of the deep crustal structure of the Qiangtang terrane using magnetotelluric imaging, *Tectonophysics*, **661**, 180–189.
- Zeyen, H., P. Ayarza, M. Fernandez, and A. Rimi (2005), Lithospheric structure under the western African-European plate boundary: A transect across the Atlas Mountains and the Gulf of Cadiz, *Tectonics*, **24**, TC2001, doi:10.1029/2004TC001639.
- Zhang C. L., and H.-bo Zou (2013), Comparison between the Permian mafic dykes in Tarim and the western part of Central Asian Orogenic Belt (CAOB), NW China: Implications for two mantle domains of the Permian Tarim Large Igneous Province, *Lithos*, **13**–27.
- Zhang, C. L., M. Santosh, H. B. Zou, Y. G. Xu, G. Zou, Y. G. Dong, R. F. Ding, and H. Y. Wang (2012), Revisiting the “Irish tectonic belt”: Implications for the Paleozoic evolution of the Altaid orogen, *J. Asian Earth Sci.*, **53**, 117–133.
- Zhang, H., D. Zhao, J. Zhao, and Q. Xu (2012), Convergence of the Indian and Eurasian plates under eastern Tibet revealed by seismic tomography, *Geochem. Geophys. Geosyst.*, **13**, Q06W14, doi:10.1029/2012GC004031.
- Zhang, Z., S. Klemperer, Z. Bai, Y. Chen, and J. Teng (2011), Crustal structure of the Paleozoic Kunlun orogeny from an active-source seismic profile between Moba and Guide in East Tibet, China, *Gondwana Res.*, **19**, 994–1007.
- Zhang, Z., Y. Wang, G. A. Houseman, T. Xu, Z. Wu, X. Yuan, Y. Chen, X. Tian, Z. Bai, and J. Teng (2014a), The Moho beneath western Tibet: Shear zones and eclogitization in the lower crust, *Earth Planet. Sci. Lett.*, **408**, 370–377.
- Zhang, Z., et al. (2014b), Geophysical constraints on the link between cratonization and orogeny: Evidence from the Tibetan Plateau and the North China Craton, *Earth Sci. Rev.*, **130**, 1–48.
- Zhao, J., G. Liu, Z. Lu, X. Zhang, and G. Zhao (2003), Lithospheric structure and dynamic processes of the Tianshan orogenic belt and the Junggar basin, *Tectonophysics*, **376**, 199–239.
- Zhao, J. M., et al. (2010), The boundary between the Indian and Asian tectonic plates below Tibet, *Proc. Natl. Acad. Sci. U.S.A.*, **107**(25), 11,229–11,233, doi:10.1073/pnas.1001921107.
- Zhao, W., et al. (2011), Tibetan plate overriding the Asian plate in central and northern Tibet, *Nat. Geosci.*, **4**, 870–873, doi:10.1038/NGEO1309.
- Zheng, J., S. Y. O'Reilly, W. L. Griffin, F. Lu, M. Zhang, and N. J. Pearson (2001), Relict refractory mantle beneath the eastern North China block: Significance for the lithosphere evolution, *Lithos*, **57**, 43–66.
- Zhou, H., and M. A. Murphy (2005), Tomographic evidence for wholesale under-thrusting of India beneath the entire Tibetan plateau, *J. Asian Earth Sci.*, **25**, 445–457.



# **Geophysical-petrological model of the crust and upper mantle in the India-Eurasia collision zone**

Lavinia Tunini<sup>1</sup>, Ivone Jiménez-Munt<sup>1</sup>, Manel Fernandez<sup>1</sup>, Jaume Vergés<sup>1</sup>, Antonio  
Villaseñor<sup>1</sup>, Massimiliano Melchiorre<sup>1</sup>, Juan Carlos Afonso<sup>2</sup>

<sup>1</sup>Institute of Earth Sciences Jaume Almera, ICTJA-CSIC, Barcelona, Spain

<sup>2</sup>GEMOC-CCFS Department of Earth and Planetary Sciences, Macquarie University, North Ryde  
NSW, Australia

## **Content of this file:**

Supplementary Material text and Figures captions (from S1 to S7)

## **Introduction:**

This supporting information provides the intermediate stages of the modeling flow described in the main text. It helps the reader to understand the step-by-step procedure which leads to the Best-Fit-Models.

## Supplementary Material

The objective of this Supplementary Material is to show the procedure followed in modeling the lithospheric structure. We are showing some of the intermediate modeling steps before obtaining the best fit model. We started with a 1D mantle geometry model (i.e. flat-LAB and homogeneous composition for the lithospheric mantle), and then we added different model complexities (lithospheric thickness variations and mantle compositional heterogeneities) as required to fit the observables (gravity, geoid, elevation, surface heat flow, geothermometric data and tomography). For each model, we show the calculated surface geophysical observables, the temperature distribution and the P-wave seismic anomaly. The Root Mean Square Error (RMSE) is calculated for the gravity anomaly, geoid, and elevation of each model (values shown in all figures in panels a-d).

### I. Intermediate modeling stages along A-B profile

Here we present the modeling results along the western profile A-B (Fig. 1) obtained in different steps until reaching the final model. We started with a model where the lithospheric thickness is the same all along the profile (*Model 0*, Section I.1). Section I.2 shows the effect of introducing lithospheric mantle thickness variations, while Section I.3 quantifies the contribution to the observables of the lateral heterogeneities in the mantle composition. The resulting RMSE and deviation of gravity, geoid and topography for each model are shown in Figure 8.

The crustal model used in all the experiments presented below is the one described in Section 5.1, where each crustal body is defined by its own set of thermo-physical parameters as detailed in Table 2. Note that the P-wave seismic anomaly is always calculated relative to a column located north of the Tian Shan, at 1910 km distance in the profile.

#### I.1 Flat LAB (Model-0)

*Model-0* is characterized by a 250-km-thick lithosphere with homogeneous mantle composition. In agreement with the age of the last tectono-thermal event (Artemieva, 2006), we consider a neo-Proterozoic lithospheric mantle (Mantle-1, Table1), the modeling results are shown in Fig. S1.

The model matches the general trends of elevation and potential fields, but the misfits are locally considerable. The calculated Bouguer anomaly is overestimated in the Tarim Basin

showing ~100 mGal of misfit. The calculated geoid height is up to 10 m higher than the observed in the northern part of the basin. The Junggar accretionary belt and Altai regions call for a higher density to fit the discrepancies of ~100 mGal in the Bouguer anomaly and ~1000 m in elevation. Additionally, the calculated mantle seismic velocities are too low (Fig. S1f) to correctly reproduce the strong positive Vp-anomalies (0.5-4 %) shown by seismic tomography (Fig. S1g).

Misfits show long wavelengths and affect the whole profile thus suggesting lateral variations of the lithospheric mantle structure (in thickness and/or composition).

## **I.2 Lithospheric mantle thickness variations (Model-1)**

*Model-1* (Fig. S2) shows lateral lithosphere thickness variations. From SW to NE, the resulting LAB deepens from 220 km below the Himalayan foreland basin to 295 km below the Kunlun Shan; shallowing to ~240 km below the Tarim Basin and then deepening again to ~260 km below the Tian Shan. Further north, the base of the lithosphere progressively deepens from ~260 km depth below the Junggar region to ~280 km below the Altai range.

The results show that topography and gravity anomaly are slightly sensitive to variations of the LAB-topography in a model with a very thick crust and lithosphere mantle as along A-B profile. Afonso et al. (2008) explain that, while the geoid height is more sensitive to deeper density anomalies and to the LAB topography, the gravity anomaly is more sensitive to shallow density anomaly distribution, at crustal or subcrustal depths. *Model-1* shows small discrepancies in the Bouguer anomaly, mainly localized in the northern tip of the profile (Junggar accretionary belt and Altai Range), and an almost perfect fit of the geoid height (1.72 m misfit).

Overall, *Model-1* shows two unresolved problems: 1) large misfits (up to 1000 m) in the modeled topography of the northern half of the profile; and 2) failure in reproducing the Vp-anomalies of the lithospheric mantle (Figs. S2f and S2g). To overcome these discrepancies, a seismically faster lithospheric mantle is required below the Tibet, whereas the mantle below the Tarim Basin and the CAO region must be faster and denser.

## **I.3 Heterogeneous mantle composition (Models 2 to 4)**

*Model-0* and *Model-1* consider a homogenous mantle composition throughout the profile, but the results evidence some misfits with the geophysical observables. The A-B transect crosses

distinct lithospheric terrains that were accreted at different times to the ancient Eurasian margin and subsequently deformed by the Cenozoic collisional events. The India-Eurasia collision triggered lithospheric thickening processes, subductions, upwelling of hot asthenosphere material, and related mantle processes (Yin and Harrison, 2000; Tapponnier et al., 2001; Jiménez-Munt and Platt, 2006; Guillot and Replumaz, 2013; and reference therein), which affected the thermal and compositional structure of the lithosphere. Thus, mantle compositional heterogeneities are likely expected in the lithosphere of the India-Eurasia collision zone.

*Model-2* (Fig. S3) incorporates a fertile mantle composition in the deepest portion of Tarim lithosphere, with a content in major oxides (NCFMAS set) equivalent to the primitive mantle of the underlying asthenosphere (Mantle 2-PUM, Table 1). Mantle-2 composition is richer in  $\text{Al}_2\text{O}_3$  and CaO with respect to Mantle-1 resulting in a denser and seismically faster mantle. Mantle-2 allows matching reasonably well the flat topography of the Tarim Basin but it fails in reproducing the strong positive P-wave anomaly of the lithospheric mantle beneath Tibetan Plateau and Tarim Basin (Figs. S3f and S3g). To the north, the Junggar and Altai regions still call for a denser lithospheric mantle to fit the topography and gravity anomaly.

*Model-3* (Fig. S4) considers a different lithospheric mantle composition below the Junggar and Altai regions. The observables require a mantle composition resulting in a higher density in this sector and, at the same time, in slower P-wave velocities relative to the Himalayan-Tibetan Plateau and Tarim Basin. Three mantle xenoliths and two magmatic dikes localities have been analyzed in the study area (Fig. 1; Song et al., 2007; Bagdassarov et al., 2011; Zhang and Zou, 2013; Chen et al., 2014). The composition inferred by these xenoliths does not satisfy the characteristics of denser and slower P-wave, and then, they do not fit the observables. A possible reason is that these xenoliths are not representative of the lithospheric mantle because the samples have been re-worked during their emplacement. Therefore, we referred to the petrological PetDB database (<http://www.earthchem.org/petdb>) to look for realistic fertile mantle compositions worldwide that could fit our model. Mantle-3 (Table 1) is characterized by an enrichment in FeO relative to MgO with respect to Mantle-1 ( $\text{Mg\#}=88.16$  relative to  $\text{Mg\#}=90.6$  of Mantle-1). This compositional change yields an increase of the amplitude of the P-wave positive anomaly below the Himalaya range, the Tibetan Plateau and the Tarim Basin relative to the CAOBL lithospheric mantle and reduces the RMSE of the surface observables. However, the resulting P-wave anomalies in the northern part of the profile (Junggar and Altair regions) are inverted with respect to the tomography image.



*Model-4* (Fig. S5) improves the previous modeling results by introducing a different lithospheric mantle composition below the Junggar Basin. With respect to the adjacent lithospheric mantle portions, Mantle-4 (Table 1) shows an intermediate content in Fe and Al and a Ca-enrichment. This allows reducing the mantle seismic velocities without changing the density significantly. The misfits in the potential fields are noticeably reduced with respect to *Model-3* and the distribution of the P-wave anomalies reasonably matches the seismic tomography. These compositional changes however, cannot account for the clear negative P-wave anomaly (up to -1%) below 250 km depth in the Tarim Basin imaged by seismic tomography (i.e. in the asthenospheric domain, Fig. S5g). The absence of large differences in the lithospheric thickness combined with the homogeneous chemical composition of the asthenosphere results in small lateral velocity variations within the asthenosphere ( $\sim 0.1$  km/s, corresponding to a  $V_p$ -anomaly of  $\sim 0.2\%$ ).

In Section 5 of the main text, we show that the negative seismic anomaly below 250 km depth in the Tarim Basin can be reproduced by incorporating a temperature anomaly of 60 °C at sublithospheric levels (best fit model, Fig. 6 and 7).

## II. Intermediate modeling stages along C-D profile

The above described modeling procedure has been applied to the eastern profile C-D (Fig. 1). We have considered the same crustal structure provided by Jiménez-Munt et al. (2008), with small differences in the Moho depth related to new data supplied by the most recent works (Yue et al., 2012; Zhang et al., 2011).

*Model-0-E* (Fig. S6) shows the results after considering a flat LAB geometry at 200 km depth. The lithospheric mantle composition is the same as that used in the western profile (Mantle-1, Table 1).

The calculated topography (Fig. S6d) is overestimated by  $\sim 1000$  m in the Himalayan-Southern Tibetan Plateau and underestimated by 200-600 m in the northern Plateau (from BNS and KF discontinuities). The calculated potential fields also show considerable misfits (up to 40 mGal in Bouguer anomaly and up to 20 m in geoid height).

The calculated temperature distribution (Fig. S6e) shows a significant upward deflection of the isotherms below the Himalayan front. The southern part of the Tibetan Plateau (Himalaya range and Lhasa terrain) is characterized by a hotter lithospheric mantle than in the northern part, which is translated into a strong negative ( $< -1\%$ )  $V_p$ -anomaly (Fig. S6f). In contrast, P-

wave tomography models show a high positive Vp anomaly beneath the Himalayan Front and Thrust Belt dipping towards the Lhasa terrane (Fig. S6g) which has been interpreted as the subduction of the Indian plate beneath the Tibetan Plateau.

*Model-1-E* (Fig. S7) incorporates lateral variations in the LAB topography showing depth values of 190 km in the Himalayan foreland, 270 km in the Himalaya range and Lhasa terrain, 130 km in the Qiantang, and 210 km in the Qaidam Basin, Qilian Shan and North China block. This lithosphere geometry would explain the geoid height and the gravity anomaly with a RMSE of only 3.86 m and 25.04 mGal, respectively. This model accounts for part of the high Vp anomaly of the Indian underthrusting (Fig. S7f), but fails in reproducing the large positive anomaly (up to 4%) beneath the Himalaya and Lhasa terrane imaged by tomography models (Fig. S7g). Moreover, the model predicts a too seismically slow mantle beneath the Qiantang terrane (Fig. S7f).

The final model (See Section 6.2 and Fig. 9) incorporates lateral variations in the lithospheric mantle composition to refine the calculated velocity anomalies.

## Supplementary Material figure captions

**Fig. S1.** *Model-0*, western profile. Modeling results considering a flat LAB at 250 km depth with homogeneous lithospheric mantle composition. a) Surface heat flow, b) Bouguer gravity anomaly, c) Geoid height, d) Topography. Blue lines represent the calculated values from the model. Red dots denote measured data, and vertical bars denote the standard deviation calculated on a strip of 50 km width (500 km for surface heat flow). e) Temperature distribution, number 1 and PUM indicate the chemical composition (Table 1). f) P-wave velocity anomalies relative to the column located at 1910 km distance along the profile (see details on the text). g) P-wave seismic tomography model (described in section 4.3). MCT = Main Central Thrust; MFT = Main Frontal Thrust; NTST = Northern Tian Shan Thrust; STST = Southern Tian Shan Thrust.

**Fig. S2.** *Model-1*, western profile. Modeling results considering LAB topography variations and homogeneous lithospheric mantle composition. Legend as in Figure S1.

**Fig. S3.** *Model-2*, western profile. Modeling results considering LAB topography variations and two different lithospheric mantle compositions (numbers refer to Table 1). Legend as in Figure S1.

**Fig. S4.** *Model-3*, western profile. Modeling results considering LAB topography variations and three different lithospheric mantle compositions (numbers refer to Table 1). Legend as in Figure S1.

**Fig. S5.** *Model-4*, western profile. Modeling results considering LAB topography variations and four different lithospheric mantle compositions (numbers refer to Table 1). Legend as in Figure S1.

**Fig. S6.** *Model-0-E*, eastern profile. Modeling results considering a flat LAB at 200 km depth with homogeneous lithospheric mantle composition. a) Surface heat flow, b) Bouguer gravity anomaly, c) Geoid height, d) Topography. Blue lines represent the calculated values from the model. Red dots denote measured data and vertical bars denote the standard deviation calculated on a strip of 50 km width (500 km for surface heat flow). e) Temperature distribution, number 1 and PUM indicate the chemical composition (Table 1). f) P-wave velocity anomalies relative to a column located at 1800 km distance along the profile (see details on the text). g) P-wave seismic tomography model (described in section 4.3). BNS =

Bangong Nuijiang Suture; IYS = Indus-Yarlung Suture; JS = Jinsha Suture; KS = Kunlun Suture; MFT = Main Frontal Thrust; NBT = North Border Thrust.

**Fig. S7.** *Model-1-E*, eastern profile. Modeling results considering LAB topography variations and homogeneous lithospheric mantle composition. Legend as in Figure S6.



# **Geophysical-petrological model of the crust and upper mantle in the India-Eurasia collision zone**

Lavinia Tunini<sup>1</sup>, Ivone Jiménez-Munt<sup>1</sup>, Manel Fernandez<sup>1</sup>, Jaume Vergés<sup>1</sup>, Antonio  
Villaseñor<sup>1</sup>, Massimiliano Melchiorre<sup>1</sup>, Juan Carlos Afonso<sup>2</sup>

<sup>1</sup>Institute of Earth Sciences Jaume Almera, ICTJA-CSIC, Barcelona, Spain

<sup>2</sup>GEMOC-CCFS Department of Earth and Planetary Sciences, Macquarie University, North Ryde  
NSW, Australia

## **Content of this file:**

Supplementary Material Figures from S1 to S7.

## **Introduction:**

This supporting information provides the figures related to the Supplementary Material text file.

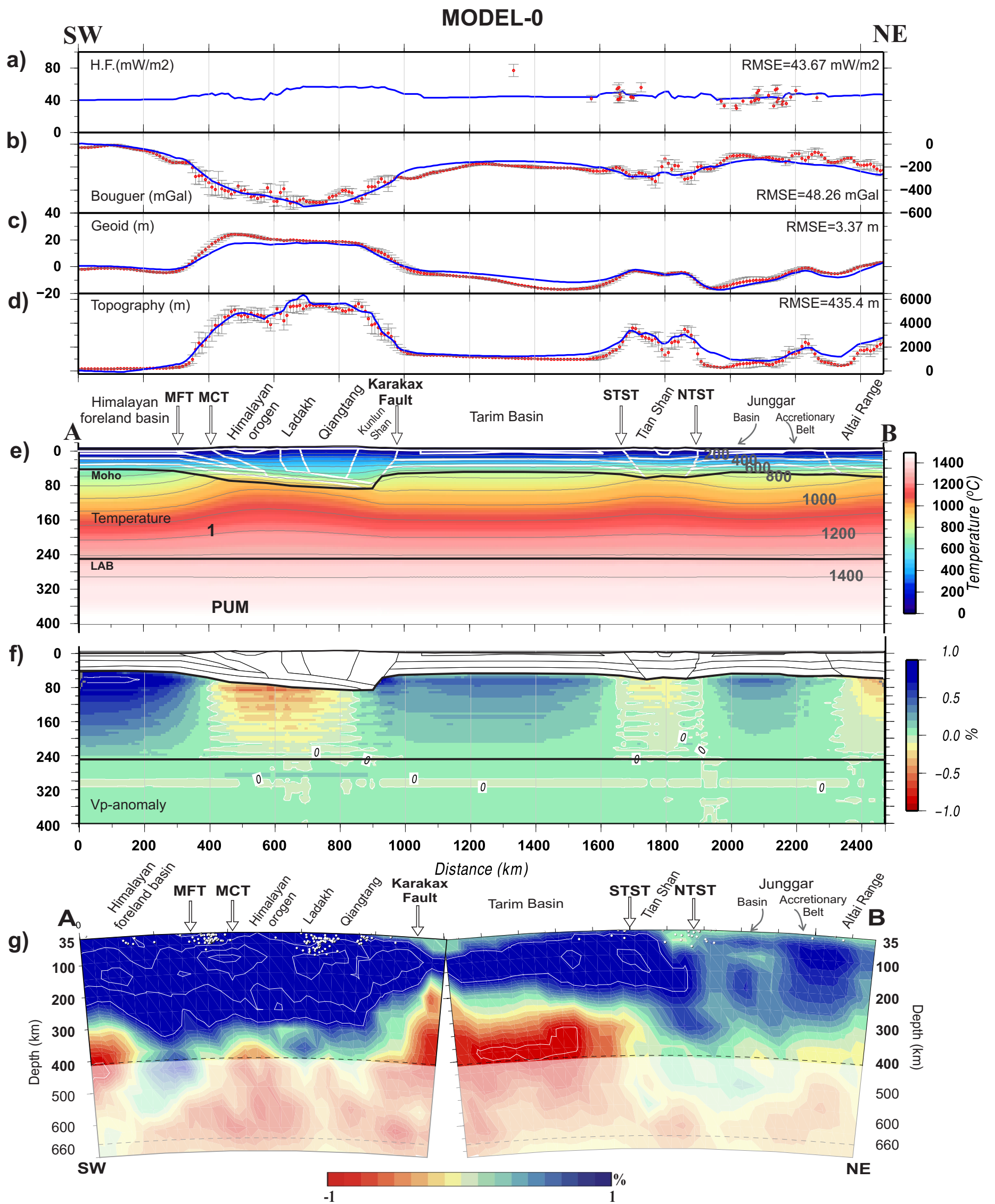


Figure S1



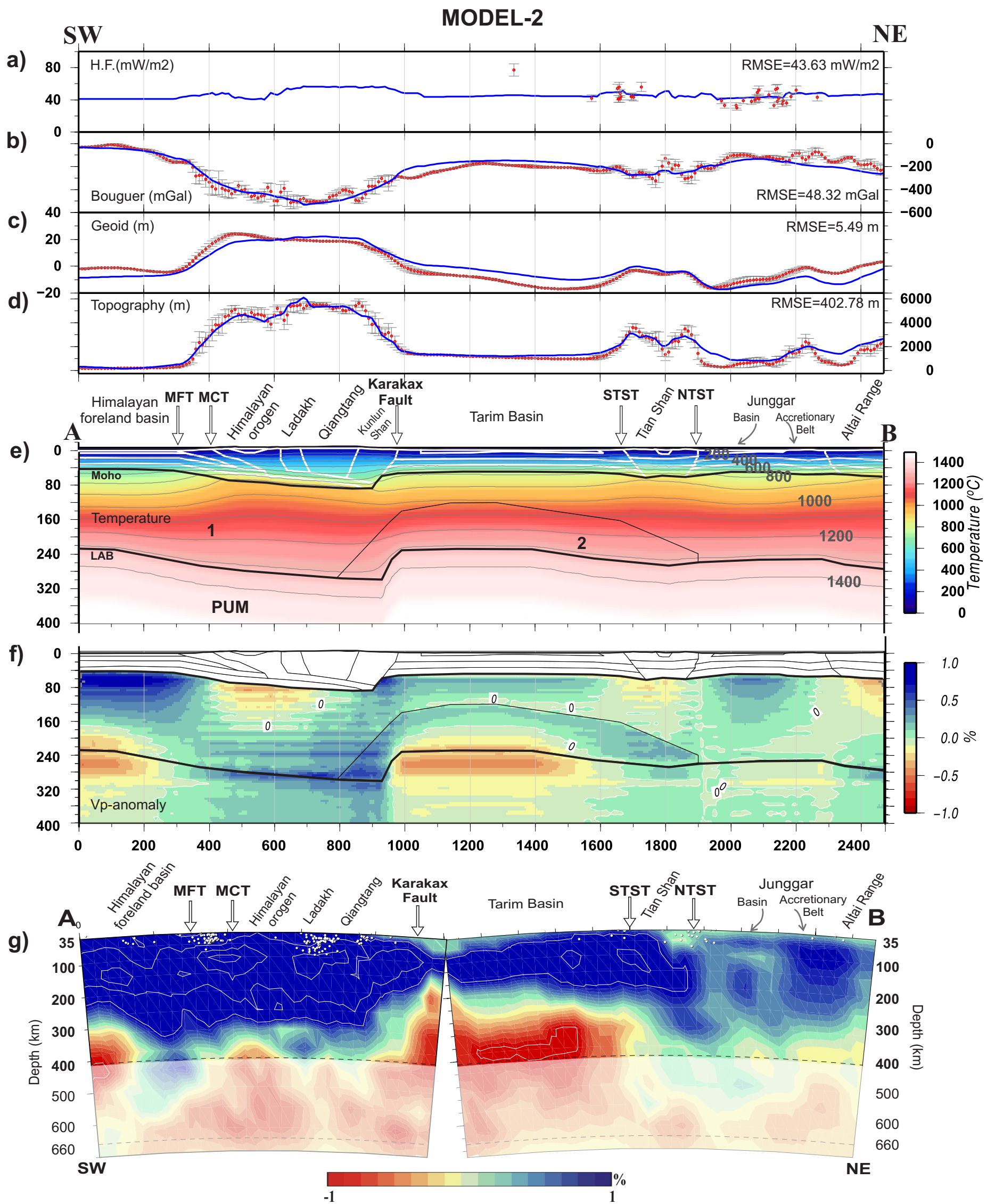


Figure S3



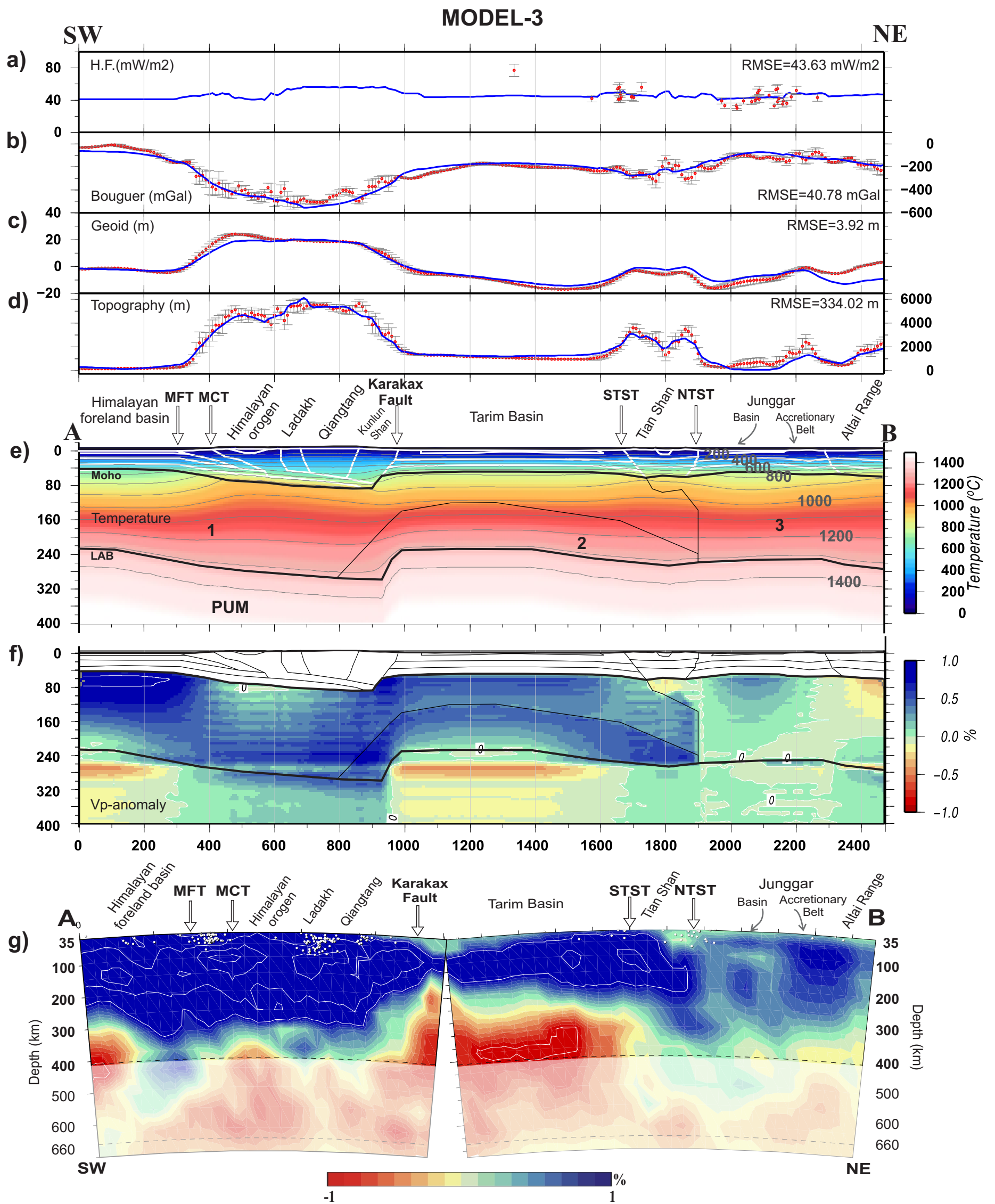


Figure S4





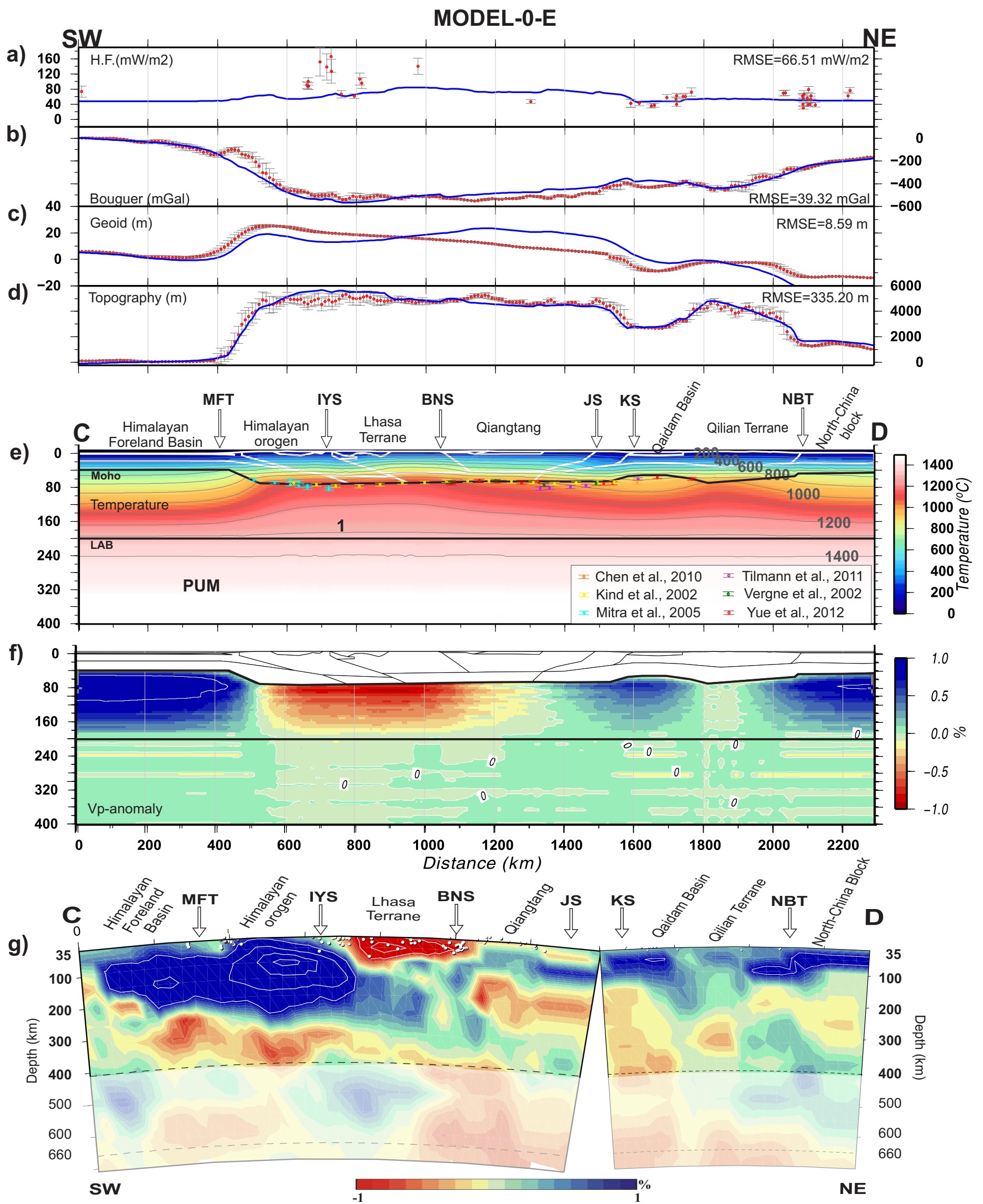


Figure S6

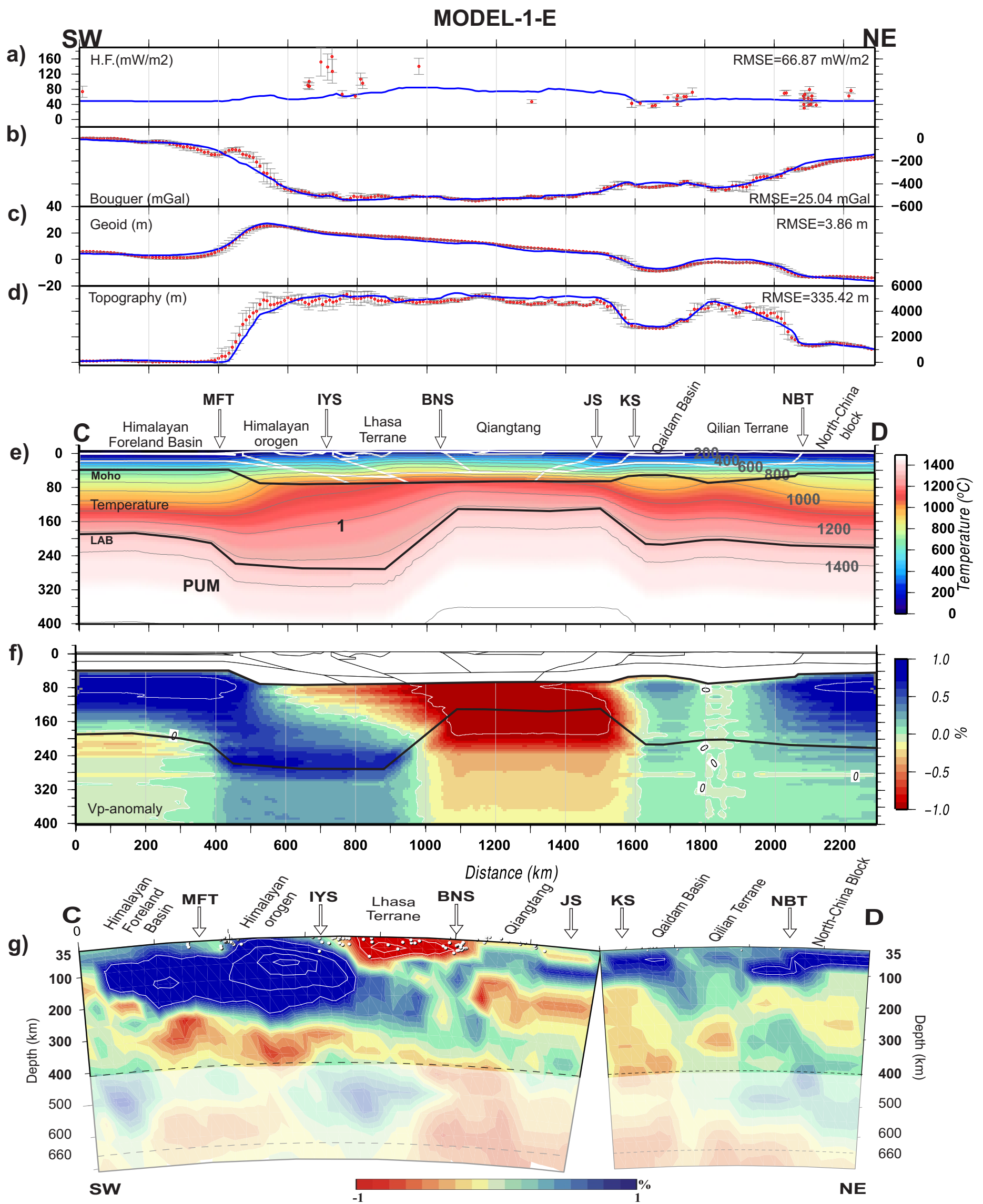


Figure S7